MNRAS 000, 1–?? (2020) Preprint 10 February 2022 Compiled using MNRAS LATEX style file v3.0

A *NuSTAR* confirmation of the 36 ks hard X-ray pulse-phase modulation in the magnetar 1E 1547.0−5408

Kazuo Makishima,[1,2,3]⋆ Teruaki Enoto,[4] Hiroki Yoneda,[3] and Hirokazu Odaka[2]
[1] *Kavli Institute for the Physics and Mathematics of the Universe (WPI), The University of Tokyo, 5-1-5 Kashiwa-no-ha, Kashiwa, Chiba, Japan 277-8683*
[2] *Department of Physics, The University of Tokyo, 7-3-1 Hongo, Bunkyo-ku, Tokyo, Japan 113-0033*
[3] *High Energy Astrophysics Laboratory, and MAXI Team, RIKEN, 2-1 Hirosawa, Wako, Saitama, Japan 351-0198*
[4] *Extreme Natural Phenomena RIKEN Hakubi Research Team, Cluster for Pioneering Research, RIKEN, 2-1 Hirosawa, Wako, Saitama, Japan 351-0198*

Accepted 2021 January 15. Received 2021 January 15; in original form 2020 September 24

ABSTRACT

This paper describes an analysis of the *NuSTAR* data of the fastest-rotating magnetar 1E 1547−5408, acquired in 2016 April for a time lapse of 151 ks. The source was detected with a 1–60 keV flux of 1.7×10^{-11} ergs s^{-1} cm^{-2}, and its pulsation at a period of 2.086710(5) sec. In 8–25 keV, the pulses were phase-modulated with a period of $T = 36.0 \pm 2.3$ ks, and an amplitude of ~ 0.2 sec. This reconfirms the *Suzaku* discovery of the same effect at $T = 36.0^{+4.5}_{-2.5}$ ks, made in the 2009 outburst. These results strengthen the view derived from the *Suzaku* data, that this magnetar performs free precession as a result of its axial deformation by $\sim 0.6 \times 10^{-4}$, possibly caused by internal toroidal magnetic fields reaching $\sim 10^{16}$ G. Like in the *Suzaku* case, the modulation was not detected in energies below ~ 8 keV. Above 10 keV, the pulse-phase behaviour, including the 36 ks modulation parameters, exhibited complex energy dependences: at ~ 22 keV, the modulation amplitude increased to ~ 0.5 sec, and the modulation phase changed by $\sim 65°$ over 10–27 keV, followed by a phase reversal. Although the pulse significance and pulsed fraction were originally very low in > 10 keV, they both increased noticeably, when the arrival times of individual photons were corrected for these systematic pulse-phase variations. Possible origins of these complex phenomena are discussed, in terms of several physical processes that are specific to ultra-strong magnetic fields.

Key words: magnetic fields— Stars: individual: 1E 1547.0−5408— Stars:magnetars — Stars:neutron — Stars: oscillations

1 INTRODUCTION

A subclass of neutron stars (NSs) called magnetars (*e.g.*, Thompson & Duncan 1995; Mereghetti 2008; Enoto et al. 2017) are thought to have extremely strong magnetic fields (MFs) with typical dipole field strengths of $B_{\rm d} = 10^{14} - 10^{15}$ G, and emit X-rays by consuming their magnetic energies. These NSs are considered to harbor, inside them, even higher toroidal MFs up to $B_{\rm t} \sim 10^{16}$ G. Evidence for this inference includes strong differential rotation which is expected to take place in the progenitor cores during their final collapse (*e.g.*, Bisnovatyi-Kogan et al. 2018), and the discovery of several objects which have rather low $B_{\rm d}$ and yet behave like magnetars (*e.g.*, Rodriguez Castillo et al.). However, the estimates of the toroidal MFs, which are confined inside the stars, have obviously remained far more difficult than those of $B_{\rm d}$, which can be made by measuring the pulse period and its time derivative (Makishima 2016).

With the Hard X-ray Detector (HXD; Takahashi et al. 2007; Kokubun et al. 2007) onboard *Suzaku*, Makishima et al. (2014) discovered a novel phenomenon that may provide direct information on $B_{\rm t}$. Specifically, through an observation of the magnetar 4U 0142+61 in 2009, they found that its 8.69 sec pulsation in the 15–40 keV energy range repeats a slow *phase modulation*, by $\sim \pm 8\%$ of a pulse cycle, with a period of $T = 55 \pm 4$ ks. In a follow-up *Suzaku* observation of the same object in 2013 (Makishima et al. 2019), this phenomenon was reconfirmed at a consistent period of $T = 54 \pm 3$ ks. Furthermore, a *NuSTAR* data set of 4U 0142+61 acquired in 2014 revealed the same modulation at $T = 54.8 \pm 5.3$ ks, although the modulation amplitude was much smaller (Makishima et al. 2019).

The $T \sim 55$ ks periodicity detected in the three observations of 4U 0142+61 has been interpreted in the following way (Makishima et al. 2014). Suppose that the star is axially deformed slightly by

$$\epsilon \equiv (I_1 - I_3)/I_3 \ , \tag{1}$$

where $\vec{I} = (I_1, I_2, I_3)$ is the moment of inertia in the coordinates $(\hat{x}_1, \hat{x}_2, \hat{x}_3)$ fixed to the star, with $\hat{x}_3$ the star's symmetry axis. Then, the period $P_{\rm pr}$ of *free-precession* of the star differs slightly from its rotation period $P_{\rm rot}$ around $\hat{x}_3$,

⋆ E-mail: maxima@rikenjp (KM)

as $P_{\rm pr} = P_{\rm rot}(1+\epsilon)$. If the star emits X-rays symmetrically around $\hat{x}_3$, we would observe regular X-ray pulses with a period of $P_{\rm pr}$ (not $P_{\rm rot}$). However, if the emission is asymmetric around $\hat{x}_3$, the beat between $P_{\rm pr}$ and $P_{\rm rot}$ will modulate the observed pulse phase slowly with a period of

$$T = P_{\rm pr}/(\epsilon \cos\alpha) \ , \tag{2}$$

which is called *slip period*. Here, α, or *wobbling angle*, is the angle between $\hat{x}_3$ and the angular momentum $\vec{L}$ which is fixed to the inertial frame. The modulation amplitude A, a fraction of P, depends positively on both α and the emission asymmetry around $\hat{x}_3$.

By identifying the observed 55 ks modulation period with this T, equation (2) indicates

$$\epsilon \cos\alpha = P_{\rm pr}/T = 1.6 \times 10^{-4}. \tag{3}$$

Assuming $\cos\alpha \sim 1$, we find $\epsilon \sim 10^{-4}$, and postulating $\epsilon > 0$ (a prolate shape), this deformation may be explained as caused by toroidal MFs hidden inside the NS. In fact, from a theoretical calculation of magnetic deformation of NSs as $\epsilon \sim 1 \times 10^{-4} (B_{\rm t}/10^{16}{\rm G})^2$ (Ioka & Sasaki 2004; Mastrano et al. 2013), the NS in 4U 0142+61 is inferred to harbor a toroidal MF of $B_{\rm t} \sim 10^{16}$ G (Makishima et al. 2014).

A second example of the same phenomenon was discovered; the fastest-rotating and highly variable magnetar 1E 1547−5408, with a pulse period of 2.07 sec. As reported by Enoto et al. (2010a), this object was observed with *Suzaku* on 2009 January 28 to 29, just a week after the onset of its very bright outburst. Analyzing the data obtained on this occasion, Makishima et al. (2016), hereafter Paper I, discovered that the pulse phase in 15–40 keV is periodically modulated with a period of

$$T = 36.0^{+4.5}_{-2.5} \ {\rm ks} \ , \tag{4}$$

and $A = 0.52 \pm 0.14$ sec which amounts to a quarter of $P_{\rm pr}$. Then, equation (2) yields $\epsilon \cos\alpha = 0.6 \times 10^{-4}$, which is of the same order as equation (3) for 4U 0142+61. Therefore, the two magnetars are suggested to have similar values of $B_{\rm t} \sim 10^{16}$ G. Furthermore, of the two characteristic spectral components of magnetars (Kuiper et al. 2006; Enoto et al. 2010b), *i.e.*, the Hard X-ray Component (HXC) and the Soft X-ray Component (SXC), only the HXC exhibited the phase modulation in either object (Makishima et al. 2014, 2019).

The results from 1E 1547−5408 are thus generally consistent with those from 4U 0142+61, and reinforce the scenario as explained above (Makishima 2016). However, the *Suzaku* pointing was a Target-of-Opportunity observation, and covered only 2.4 cycles of $T = 36$ ks. Therefore, the phase modulation in the HXC pulses could be some transient phenomena, particularly those associated with the enhanced activity, rather than a manifestation of persistent free precession. To reconfirm equation (4), it is hence needed to observe 1E 1547−5408 in quiescence, and for a considerably longer period. In fact, the object was observed again with *Suzaku* in 2010 August, 1.5 years after the first observation, but the source was already rather faint, so its HXC was detected with the HXD only marginally (Iwahashi et al. 2013). This has motivated us to use *NuSTAR* instead.

2 OBSERVATION

Based on our proposal for the *NuSTAR* cycle-1 Guest Observation Program, the present observation of 1E 1547−5408 (ObsID 30101035002) was conducted from 2016 April 23 UT 00:11:08 through April 24 UT 18:16:08, for a total time lapse of 151 ks. Through the standard data screening, the two focal-plane instruments, FPMA and FPMB, both achieved a net exposure of 83 ks. By the present observation, 1E 1547−5408 had already attained a relatively steady intensity, which is an order of magnitude lower than in the 2009 *Suzaku* observation (§ 3.1), but still considerably higher than those in 2006 (Kuiper et al. 2012; Iwahashi et al. 2013; Enoto et al. 2017; Coti Zelati et al. 2020). The acquired data were already utilised by Coti Zelati et al. (2020), hereafter CZ20, mainly with respect to the long-term source behaviour through the outburst decay.

The on-source events from FPMA and FPMB were accumulated within a circle of radius $60''$ around respective image centroids, and the background events were taken from a source-free region on the respective images. We applied dead-time corrections to the on-source data, subtracted the background, and performed vignetting corrections. The object was detected at a background-removed 3–80 keV count rate of 0.11 c s^{-1} for FPMA+FPMB, in agreement with CZ20. The arrival times of individual events were then converted to those to be measured at the Solar-system barycentre, utilizing the source position of $(\alpha^{2000}, \delta^{2000}) = (15^{\rm h}50^{\rm m}54^{\rm s}.12, -54^\circ 18' 24''.11)$, and the spacecraft orbital information.

3 BASIC DATA ANALYSIS

3.1 Spectra

Although the present paper aims at detailed timing studies of 1E 1547−5408, a brief spectral study would be necessary in order to grasp approximate spectral characteristics, and to confirm the consistency with CZ20. We hence created background-subtracted FPMA and FPMB spectra separately, and present them in Fig. 1 in the $\nu F\nu$ form. In agreement with Fig. 2 of CZ20, they exhibit a spectral shape characteristic of magnetars, consisting of the SXC and the HXC which are dominant in energies below and above ~ 12 keV, respectively.

We fitted the spectra jointly, using a model in which the HXC is expressed by a single power-law, and the SXC with a sum of two blackbody components (*e.g.*, Nakagawa et al. 2009; Enoto et al. 2011). This modeling is empirical rather than physical, and may not be a unique description of magnetar spectra in general, or of the present spectra. The fit was approximately successful with a reduced chi-square of $\chi^2/\nu = 253.1/211$, and yielded the HXC photon index as $\Gamma_{\rm h} = 0.22 \pm 0.12$. The two blackbody temperatures for the SXC were obtained as 0.61 ± 0.03 keV and 1.2 ± 0.1 keV; they are approximately in the 1:2 ratio as in many other magnetars (Nakagawa et al. 2009). These parameters are consistent with those of CZ20, although they combined the 2016 data with another data set acquired in 2019.

Using the above model fitted to the *NuSTAR* spectra, we measured the HXC flux as $F_{\rm h} = 5.6 \pm 0.3$, and the SXC flux after correcting for the absorption as $F_{\rm s} = 11.1 \pm 0.1$, both in

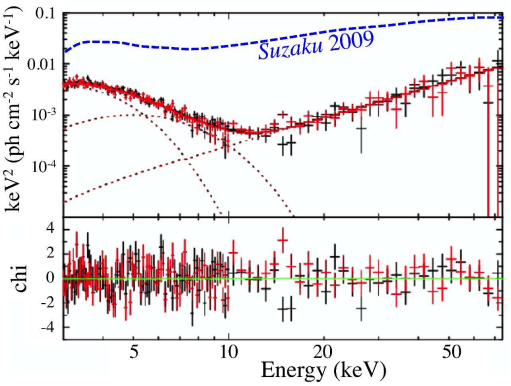

Figure 1. Background-subtracted $\nu F\nu$ spectra of 1E 1547−5408 from FMPA (black) and FPMB (red). They are jointly fitted by a model consisting of two blackbodies for the SXC, and a power-law for the HXC. The *Suzaku* spectrum taken in the 2009 outburst is superposed in a dahsed blue line, also in the $\nu F\nu$ form.

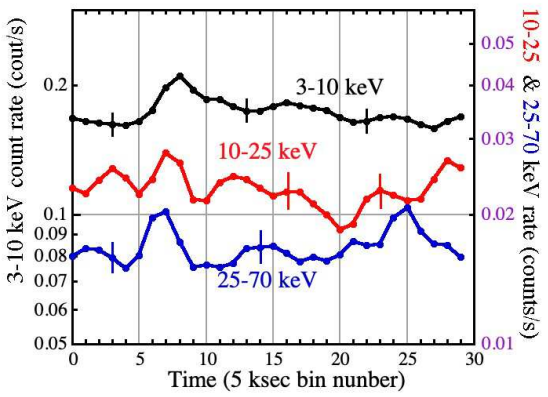

Figure 2. Background-inclusive light curves of 1E 1547−5408 from FPMA+FPMB, binned into 5 ks and corrected for dead time. Black, red, and blue respectively represent 3–10 keV (left ordinate), 10–25 keV (right ordinate), and 25–70 keV (same) events. The background rate is 1.9×10^{-3}, 1.0×10^{-3}, and 1.1×10^{-3} c s^{-1}, in the 3–10, 10–25, and 25–70 keV bands, respectively.

1–60 keV and in units of 10^{-12} erg s^{-1} cm^{-2}. The total 1–60 keV flux is hence 16.7×10^{-12} ergs s^{-1} cm^{-2}. For comparison, the 2009 *Suzaku* data gave $F_{\rm h} = 158.7$ and $F_{\rm s} = 50.6$, in the same units (Table 5 of Enoto et al. (2017)). Thus, from the 2009 observation, the source became about an order of magnitude fainter, with the HXC and SXC declining by a factor of 30 and 5, respectively. The HXC/SXC flux ratio, previously $\xi \equiv F_{\rm h}/F_{\rm s} = 3.1$ in 2009, has decreased to $\xi = 0.50 \pm 0.03$ accordingly. This decrease in ξ by a factor of ~ 6 is somewhat larger than the value of 2–3 reported by CZ20, but this can be attributed to the different energy ranges utilised for the flux definition. The two spectral measurements, in 2009 and 2019, still satisfy the empirical scaling between ξ and the characteristic age (common to the two data sets) found by Enoto et al. (2010b, 2017), within the scatter by a factor of a few which is likely to be inherent to the scaling.

Compared to the *Suzaku* 2009 spectrum superposed in Fig. 1, the present spectra are characterised not only by the reduced fluxes, but also by a clearer intensity minimum at $\sim$ 12 keV where the two spectral components cross over. This can be attributed mainly to the harder HXC; $\Gamma = 1.3$ in 2009, $\Gamma \sim 1.1$ in 2010 (Iwahashi et al. 2013), and $\Gamma = 0.2$ in the present observation. Therefore, another empirical scaling found by Enoto et al. (2010b), that older magnetars exhibit harder HXC (their Fig. 4a), may be modified into a statement that *less active magnetars show harder HXC*.

3.2 Light curves

Figure 2 presents dead-time corrected but background-inclusive light curves of 1E 1547−5408 with 5 ks binning, derived in 3–10 keV, 10–25 keV, and 25–70 keV. Here and hereafter, we use the events from FPMA and FPMB co-added together, because they provide a fully consistent pair of spectra. As clear from Fig. 1, the first band represents the SXC, whereas the latter two mainly the HXC. Thus, the object was mildly variable with typical amplitudes of $\sim \pm 20\%$, on time-scales of several tens kiloseconds. Over the bin number from 5 to 10, the source brightened by $\sim$ 30%, where the intensity maximum appears to propagate from the highest to the lowest bands in $\sim$ 10 ks. This suggests that the HXC variation causes the SXC to vary with some delay. However, a standard cross-correlation analysis among the three light curves did not yield meaningful results.

3.3 The pulsation

3.3.1 Periodograms

To study the 2.07 sec source pulsation, we utilise the Z^2 technique. Like in the conventional chi-square method, we first fold the data, at a trial period P, into a folded profile of $N_{\rm bin}$ bins, $\{C_j(P); j = 0, 1, ., N_{\rm bin} - 1\}$, and express it as

$$C_j(P) = \sum_{k=0}^{N_{\rm bin}/2} \{a_k(P)\cos(\Omega k j) + b_k(P)\sin(\Omega k j)\} \ . \qquad (5)$$

in a Fourier expansion. Here, $k = 0, 1..., N_{\rm bin}/2$ is the wave number, $\{a_k(P), b_k(P)\}$ are Fourier coefficients, and $\Omega \equiv 2\pi/N_{\rm bin}$. Then, the k-th Fourier power is obtained as

$$Q_k(P) = a_k(P)^2 + b_k(P)^2 \ .$$

Summing up Q_k from the fundamental ($k = 1$) to a specified harmonic m, and normalising the result to the total photon counts $N_{\rm tot}$, the statistical quantity Z^2_m is obtained as

$$Z^2_m(P) = \frac{1}{2N_{\rm tot}} \sum_{k=1}^{m} Q_k \ , \qquad (6)$$

of which some properties are given in Appendix A. Together with $N_{\rm bin} = 360$, we use $m = 4$, because the pulse profiles of magnetars after the demodulation analysis often exhibit three to four peaks per cycle (Makishima et al. 2019).

By applying the Z^2 technique to the background-inclusive data, we calculated periodograms, *i.e.*, the values of Z^2_4 as a function of the trial period P. The results are shown in Fig. 3, where the two harder bands used in Fig. 2 were combined into one (blue; 10–70 keV) to increase the statistics. Instead, we have included a result from an intermediate band, 8–25 keV (red), which plays an important role later on. Thus, at least in the lower two energy bands, the source pulsation is detected clearly, at a period of

$$P_0 = 2.086\ 710 \pm 0.000\ 005 \text{ sec} \ , \qquad (7)$$

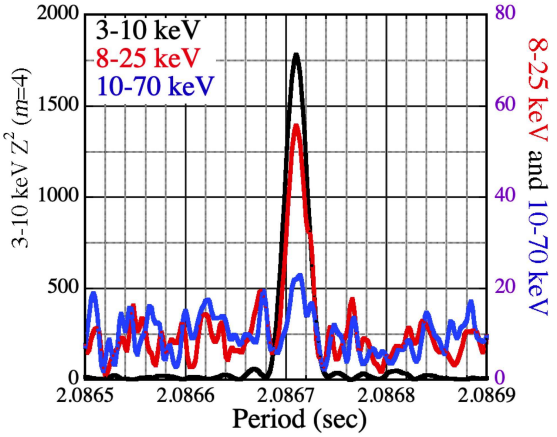

Figure 3. Periodograms calculated from the background-inclusive FPMA+ FMPB data, using the Z^2 method with $m = 4$. Black shows the result in the 3–10 keV band, with the left ordinate. Red and blue are those for the 8–25 keV and 10-70 keV bands, respectively, with the right ordinate.

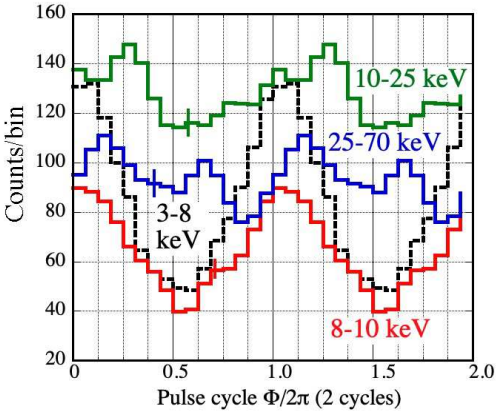

Figure 4. Time-averaged pulse profiles in 3–8 keV (black dashed), 8–10 keV (red), 10–25 keV (green), and 25–70 keV (blue), folded at P_0 and shown, with the running average, as a function of the pulse cycle $\Phi/2\pi$. The ordinate is the background-inclusive photon counts per bin, where the 3–8 keV counts are scaled to 1/10.

in full agreement with CZ20. The chance probability of this peak is estimated as 3.2×10^{-9} in 8–25 keV, before counting trials. Since the period range in Fig. 3 is covered by ~ 14 independent Fourier wave numbers, the probability becomes $\sim 4.5 \times 10^{-8}$ when considering the frequency trial numbers. This is still extremely low.

The peak at P_0 is also visible in the 10–70 keV periodogram, but its chance probability is 5×10^{-3} and ~ 0.07 before/after considering the frequency trials, respectively, and is comparable to several other peaks. Therefore, we cannot claim the pulse detection in the 25–70 keV interval.

Compared with the period of 2.072 135 ± 0.000 005 sec measured in 2009 January (Enoto et al. (2010a); Paper I), equation (7) implies that the object has been spinning down with an average rate of $\dot{P} = 6.4 \times 10^{-11}$ s s^{-1}, which is somewhat larger than the long-term average of 3.4×10^{-11} s s^{-1} in 2 years from 2009 January as measured with a dense sampling by Kuiper et al. (2012). This is however not unusual, because $\dot{P}$ of this object and of other magnetars generally fluctuates considerably.

3.3.2 Pulse profiles and the pulsed fraction

Figure 4 shows the folded pulse profiles as a function of the pulse cycle, $\Phi/2\pi$. Here, Φ is the pulse phase defined as

$$\Phi = 2\pi \ \mathrm{mod}(t/P_0) \ , \tag{8}$$

where "mod" means modulo, and t is the time as measured from a Mission Elapsed Time of 199,067,862.632 sec. The three energy intervals utilised in Fig. 3 have been re-arranged into non-overlapping four energy bands. Here and hereafter, the pulse profiles are presented after taking running averages, which combine three consecutive data bins with weights of 0.25, 0.5, and 0.25. As shown in Appendix B, this reduces the statistical errors, associated with individual data bins, to 0.61 times the Poissonian values, at the sacrifice of independence between adjacent data points.

In a similar way to equation (6), we define the pulsed fraction (PF) as

$$\mathrm{PF} = \frac{1}{N_{\rm tot}} \left[\sum_{k=1}^{4} Q_k - \sum_{k=1}^{4} Q_k^{(n)} \right]^{1/2} \ , \tag{9}$$

where $Q_{\rm k}$ again denotes the Fourier power of the profile *before taking the running average*, and $Q_k^{(n)}$ is the expected Poissionian-noise contribution. This $Q_k^{(n)}$ was evaluated via a Monte-Carlo simulation, wherein a constant pulse profile with the same average counts/bin as the actual data was randomised, 1000 times, to emulate the Poissonian noise.

For a purely sinusoidal waveform with $Q_k^{(\rm n)} \sim 0$, the PF defined in this way coincides with a more simple-minded definition of [pulse peak−pulse bottom]/average. Like Z_m^2, this PF is independent of $N_{\rm bin}$ for $N_{\rm bin} \gg m$, but unlike Z_m^2, it is also independent of $N_{\rm tot}$ as long as the pulse profile keeps a constant shape. When $Q_k^{(\rm n)}$ can be ignored, we expect, from equations (6) and (9),

$$Z_m^2(P_0) \sim \frac{N_{\rm tot}}{2} \times (\mathrm{PF})^2 \ . \tag{10}$$

Our PF definition is similar to that of CZ20, except some differences in the normalisation, and in the harmonic number employed; while they used $m = 2$, we sum up to $m = 4$ to be consistent with the Z_m^2 analysis.

Referring to Fig. 4, the PF thus defined has been found to be 48.6%, 35.4%, 10.2%, and 14.9%, in 3–8, 8–10, 10–25, and 25–70 keV, respectively. The results are consistent with Fig. 5 of CZ20, considering the difference in the definition of PF. These PF values in < 10 keV from the present data, and those measured by Kuiper et al. (2012) through the outburst decline, are higher than those derived during the 2009 outburst, 16–28% in 1–50 keV (Enoto et al. 2010a), or before (Halpern et al. 2008). In addition, contrary to the observations in 2009 where the PF increased with energy (Enoto et al. 2010a), the present PF drops markedly above ~ 10 keV, which is also seen in Fig. 5 of CZ20. Thus, the pulsed emission appears to have changed through the decay of the 2009 activity.

Figure 4 also reveals some complex energy-dependent behaviour in the pulsation. The 3–8 keV and 8–10 keV profiles

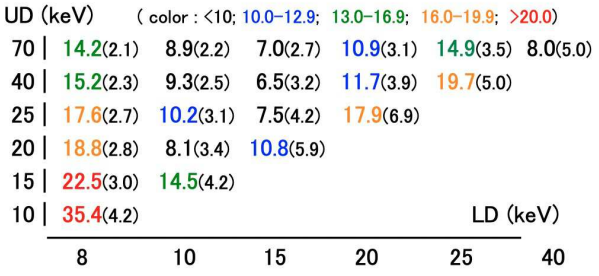

Figure 5. The PF (see text) in percent, shown as a function of the LD (abscissa) and the UD (ordinate) in a matrix form. The numbers in parenthesis give 1-sigma statistical errors, estimated by the Monte-Carlo simulation that was employed to calculate $\sum Q_k^{(n)}$ in equation (9).

have a single peak at $\Phi/2\pi \sim 0$. In 10–25 keV where the HCX becomes dominant, the pulse minimum is still kept the same at $\Phi/2\pi \sim 0.5$, but the peak at the pulse cycle ~ 0 is exceeded by a stronger peak that appeared at $\Phi/2\pi \sim 0.3$. In Fig. 5 of CZ20, this effect is observed as a phase difference, by ~ 0.15 pulse cycles, between the 10–25 keV and < 10 keV profiles. Our 25–70 keV profile shows two peaks, and neither is in phase with those in the lower energies.

To more systematically study the PF behaviour, we fixed $P = P_0$, and produced pulse profiles at finer energy bands, by changing the lower- and upper-threshold energies, abbreviated as LD and UD, respectively. The derived PF values are given in Fig. 5, on the LD vs. UD plane in a matrix form. It reconfirms the implication of Fig. 4, that the PF is rather low at intermediate energies. The figure further indicates a hint of PF increase towards the diagonal matrix line. This suggests that the pulse coherence degrades when the data are summed over wider energy ranges, possibly due to some energy dependences in the phases and/or shapes of the HXC pulses as pointed out by CZ20.

3.3.3 Dynamic pulse profiles

Although Fig. 4 averages over the total data length, the HXC pulse profile of a magnetar is known to vary on time-scales of hours (*e.g.*, Enoto et al. 2011), partially coupled with free precession (Makishima et al. 2019), as well as in months through an outburst decay (Kuiper et al. 2012). The PF would then degrade in some energy ranges, if such profile/phase changes are enhanced therein. To grasp this possibility, we use a plot to be called a *dynamic pulse profile*; it is a two-dimensional color map, where the abscissa is the pulse cycle, the ordinate shows the time lapse t, and the color represents the X-ray intensity at $(\Phi/2\pi, t)$. Using the Good Time Interval information, we correct the map for exposure in the t dimension, but not in the Φ direction where the exposure is uniform to within $\sim 2\%$. In the Φ direction, we instead apply the running average, to make the results consistent with time-integrated pulse profiles such as in Fig. 4. The obtained results are shown in Fig. 6.

The 3–6 keV dynamic pulse profile in panel (a), representing the SXC pulse behaviour, is dominated by a straight vertical ridge formed by the pulse peak, at a pulse cycle 0–0.1 in agreement with the 3–8 keV profile in Fig. 4. Except some variations in the ridge height due to the source variability (Fig. 2), the pulse phase and shape are rather constant. The pulse behaviour looks still similar in panel (b), where we narrowed the energy interval to 7.1–8.0 keV to purposely reduce the signal statistics. In contrast, the 8–10 keV result in panel (c) reveals larger pulse-phase fluctuations with time. This is likely to be intrinsic, because the energy ranges of (b) and (c) were selected to have similar (within 10%) pulse significances in terms of the pulse amplitude relative to the Poisson noise. In the two higher energy intervals, these fluctuations further increase, though due partially to increasing Poissonian errors. In Fig. 6e, an interpulse emerges at a pulse cycle ~ 0.6, in agreement with Fig. 4 (blue).

Figure 6 thus suggests that the pulse phase/shape in $\gtrsim 10$ keV fluctuates with time. This could be responsible for the pulse-coherence degradation seen in these energies (Fig. 5). Furthermore, if the fluctuation is energy dependent, the degradation would be enhanced when the data are summed over wider energy intervals.

4 DETAILED PULSATION ANALYSIS

If the time- and energy-dependent variations in the HXC pulse properties (§ 3.3) are of sporadic nature, there would be little hope to recover the pulse coherence. However, if they are of systematic nature, and quantified as functions of time and energy, we may recover the pulse coherence through corrections for the systematic effects. This is similar to the case of a pulsar in a binary, where the pulsation generally becomes much more significant when the arrival times of individual photons are corrected for the pulsar's binary motion. This section is devoted to such attempts.

4.1 Demodulation analysis of the 8–25 keV data

Putting off the energy dependent corrections to § 4.2, we first consider the time dependence, assuming that the HXC pulse-phase variation is periodic as actually observed in 4U 0142+61 (§ 1), and 1E 1547−5408 in 2009 (Paper I). To search for any preferred periodicity (including 36 ks in particular) in the pulse-phase fluctuation in the present data, we perform a so-called demodulation analysis (Makishima et al. (2014); Paper I; Makishima et al. (2019)). We start this analysis with the 8–25 keV energy band, where the pulse is suggested to fluctuate with time as in panels (c) and (d) of Fig. 6, but the PF is still not too low, 17.6% (Fig. 5).

The demodulation analysis postulates that the arrival time t of each pulse from the pulsar deviates from an exact periodicity by an amount

$$\delta t = A \sin\{\Psi(t) - \psi\} \ , \tag{11}$$

where

$$\Psi(t) = 2\pi \ \mathrm{mod}(t/T) \tag{12}$$

is the modulation phase defined in a similar way to Φ of equation (8), $T \gg P$ and $A < P$ describe the period and amplitude of the assumed pulse-phase modulation, respectively, and ψ is the initial modulation phase (with the sign reversed). Then, by shifting the arrival times t of individual photons (instead of those of individual pulses) back by $-\delta t$, we re-calculate the pulse periodogram, and search for a triplet (T, A, ψ) that maximizes $Z^2_{\rm m}(P)$ at $P \sim P_0$ of equation (7).

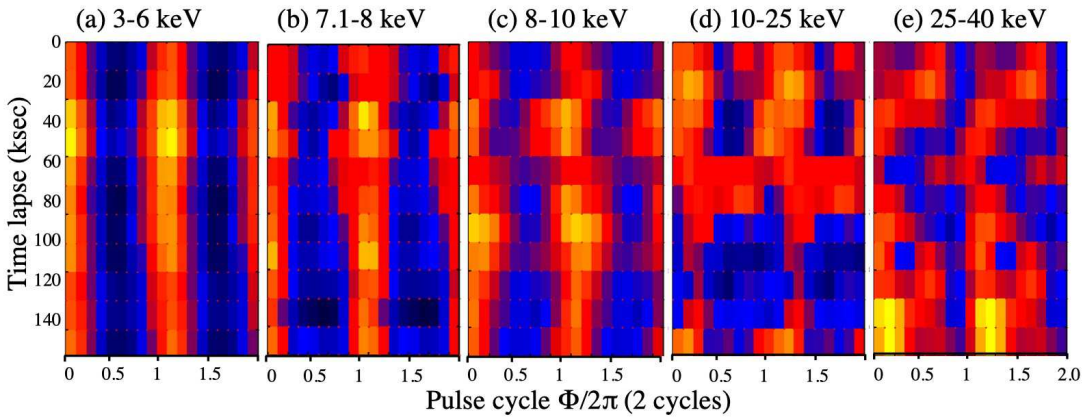

Figure 6. Dynamic pulse profiles (see text) in 5 energy bands. The color indicates the background-inclusive intensity, increasing from black, blue, red, to yellow. The abscissa is the pulse cycle $\Phi/2\pi$ (2 cycles), whereas the ordinate is the time lapse in ks running downwards from the start to the end of the observation. The exposure correction and the running averages are applied in the t and Φ directions, respectively.

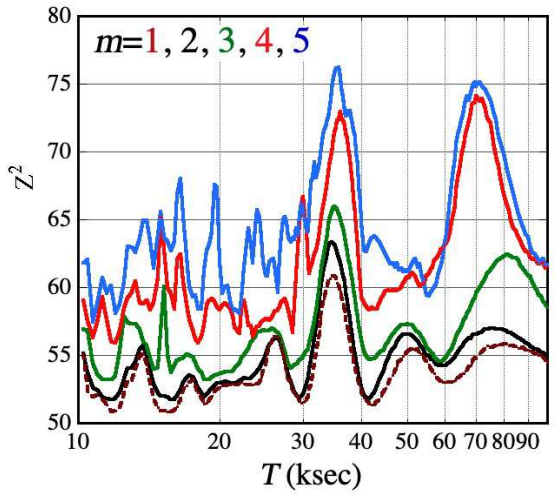

Figure 7. The DeMDs for the 8–25 keV data. The abscissa shows the assumed modulation period T, wheres the ordinate represents the maximum Z^2_m when A, ψ, and P are optimized at each T. From bottom to top, the curves represent $m = 1$ (dashed brown), $m = 2$ (black), $m = 3$ (green), $m = 4$ (red), and $m = 5$ (blue).

In practice, T was varied from 10 ks to 100 ks with a step of 0.2–1.0 ks, A from 0 to 0.6 sec ($\gtrsim P/4$) as in Paper I, with a step of mainly 0.01 sec, and ψ from 0 to 360° with a 10° step. For each triplet, the pulse period P was scanned over the error range of equation (7) with a 2 μ sec step.

Figure 7, which we call a *demodulation diagram* (hereafter DeMD), summarises the results of this analysis using the 8–25 keV data. The abscissa represents T, and the ordinate the maximum Z^2_m obtained at each T, when A, ψ, and P are varied within the respective scan ranges. The results with $m = 1$ to 5 all reveal prominent peaks at $T \sim 36$ ks. Their widths of $\Delta T \sim 8$ ks, which satisfy $\Delta T/T \sim T/151$, are consistent with being determined by the data length of 151 ks. For $m = 4$ and $m = 5$, an additional peak is seen at $T \sim 72$ ks, which is just twice that of the main peak.

When selecting $m = 4$ as a representative, the peak at 36 ks is characterised by

$$T = 36.0 \pm 2.3 \text{ ks} \ , \quad A = 0.19 \pm 0.06 \text{ s} \ , \quad \psi = 150^\circ \pm 25^\circ \quad (13)$$

and

$$Z^2_4 = 72.95 \quad , \quad \delta Z^2_4 = 17.23 \quad (14)$$

together with P of equation (7). Here, δZ^2_m is the increment in Z^2_m relative to the value before the demodulation, and provides a measure of the pulse-significance increase (Appendix A). These parameters obtained in the demodulation analysis are summarised in Table 1, together with those obtained later in other energy intervals. As given there, the demodulation has increased the 8–25 keV PF from 17.6% to 20.7%, reflecting equation (10). Hereafter, we keep using $m = 4$, because δZ^2_4 in equation (14) is considerably larger than $\delta Z^2_1 = 10.22$, $\delta Z^2_2 = 11.94$, and $\delta Z^2_3 = 12.58$. (Although $\delta Z^2_5 = 19.89$ is still larger, the DeMD becomes noisier.)

As explained in Appendix C, the errors associated with the demodulation parameters have been estimated as the range where the Z^2_4 values stay between the maximum and the maximum minus 4.72. This updates the more conventional method of error estimation, adopted so far by Makishima et al. (2014), Paper I, and Makishima et al. (2019).

The value of T of the DeMD peak in Fig. 7 (equation 13) is consistent with equation (4) derived with *Suzaku*. Moreover, as detailed in Appendix D, we find a chance probability of $\sim 0.5\%$ for a Z^2_4 peak higher than equation (14) to appear at T that is consistent with equation (4). We hence conclude that the 36 ks pulse-phase modulation detected with *Suzaku* has been reconfirmed with *NuSTAR*, at least in the 8–25 keV energy band. Although A is much smaller than the *Suzaku* result of $A = 0.52 \pm 0.14$ sec (Paper I), this would not be a problem, because marked changes in A have been observed from 4U 0142+61 (Makishima et al. 2019).

To visualise the 36 ks pulse-phase modulation, Fig. 8 presents another form of two-dimensional X-ray count-rate map, which we call a *double-folded map*. It is obtained by sorting the photons into two dimensions, where the abscissa $\Phi/2\pi$ again specifies the pulse cycle, and the ordinate $\Psi/2\pi$ the modulation cycle modulo T. As before, the exposure correction is applied only in the Ψ-dimension, and the running average only in the Φ-dimension. It is thus similar to Fig. 6,

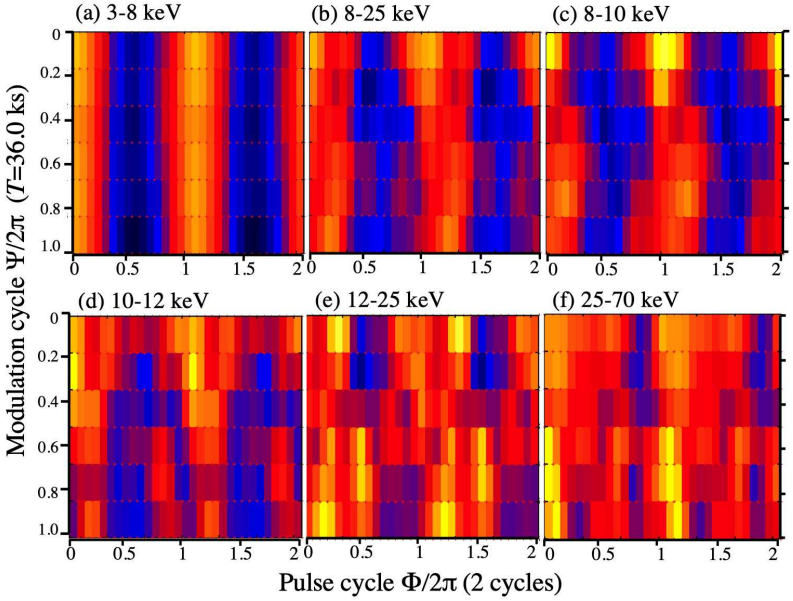

Figure 8. Double-folded maps in 6 energy bands, each shown on a plane formed by the pulse cycle $\Psi/2\pi$ and the cycle $\Psi/2\pi$ of the 36 ks modulation periodicity. The color coding, the exposure correction, and the running average are the same as in Fig. 6.

but differs in the ordinate. The 3–8 keV map in panel (a) shows a straight pulse ridge running at $\Phi/2\pi \sim 0.05$, as expected from panels (a) and (b) of Fig. 6. In contrast, in panel (b) using the 8–25 keV photons, the ridge is observed to wiggle laterally by ± 0.1 pulse cycles, in agreement with equation (13). This is the 36 ks pulse-phase modulation in 8–25 keV. The other panels of Fig. 8 are utilised later.

4.2 Demodulation in various energy bands

In § 4.1, we reconfirmed the *Suzaku* result using the *NuSTAR* data, because Z_4^2 (and the associated PF) increased significantly via demodulation with $T = 36$ ks. However, these are limited to the 8–25 keV band. We hence attempted the demodulation analysis in other energy ranges.

4.2.1 Results in < 10 keV

In the 3–8 keV energy band where the SXC dominates, neither Fig. 6 nor Fig. 8 give evidence of significant pulse-phase fluctuations. To be more quantitative, we calculated the DeMD in 3–8 keV, and show it in Fig. 9a. Thanks to the high signal-to-nose ratio attained by *NuSTAR*, the pulsation is strongly detected, with $Z_4^2 = 1715.7$ and the PF of 48.6%, both without demodulation. The DeMD shows several peaks, but the highest one at $T \sim 100$ ks is close, in period, to the observation length of 151 ks, so this would not be regarded as a periodic variation. Furthermore, the associated value of $A = 0.05$ sec is only 2.5% of one pulse cycle. The 2nd highest one at $T = 11.8$ ks is probably instrumental, because it is just twice the orbital period of *NuSTAR* (5.8 ks). The third one at $T \sim 45$ ks is eye catching, but it has only $\delta Z_4^2 = 6.9$, and $A = 0.03$ sec which is only 1.5% of a pulse cycle. Therefore, we regard this peak and the 4th one at $T \sim 16$ ks as due to Poisson noise. We do not see any Z_4^2 enhancement at $T \sim 36$ ks, either. Thus, the soft X-ray pulses below 8 keV,

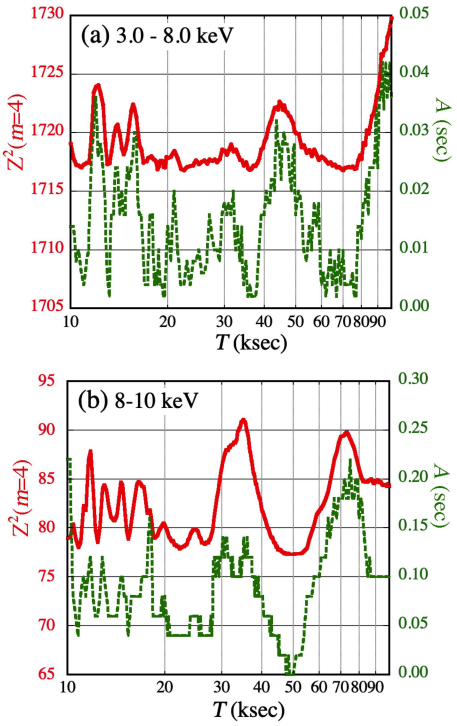

Figure 9. The $m = 4$ DeMDs in 3–8 keV (panel a) and 8–10 keV (panel b). The solid red curves show the maximum Z_4^2 values (left ordinate), whereas the dashed green curves give A (right ordinate) that maximizes Z_4^2.

dominated by the SCX, are free from pulse-phase modulations, at 36 ks or any other period studied here. We quote a typical upper limit of $A \lesssim 0.04$ sec, for the 36 ks pulse-phase modulation in 3–8 keV.

Figure 9b shows the $m = 4$ DeMD, together with the be-

Table 1. Basic pulse properties of 1E 1547−5408 in four energy intervals, as observed with *NuSTAR* in 2009.

Energy (keV)	Stage[a]	P (sec)	Z_4^2	δZ_4^2 [b]	T (ks)	A or A_0 (sec)	ψ or ψ_0 (deg)	PF [c]	Reference[d]
	No Demod.	2.086714	56.18	—	—	—	—	14.2	Fig.10 black
8–70	Simple Dem.	2.086710	68.43	12.25	34.5	0.14	170	15.9	
	EDPV	2.086708	108.38	52.20	36.0	0.51	190	20.5	
	No Demod.	2.086708	74.20	—	—	—	—	35.4	Fig.4 red
8–10	Simple Dem.	2.086710	91.11	16.91	35.0	0.12	200	39.6	Fig.9b, Fig.11c
	EDPV	(2.086710	91.81	17.61	35.0	0.43	210	40.0) [e]	
	No Demod.	2.086710	55.72	—	—	—	—	17.6	Fig.3 red
8–25	Simple Dem.	2.086708	72.95	17.23	36.0	0.19	150	20.7	Fig.7, eqs.(13),(14)
	EDPV	2.086708	92.18	36.46	36.0	0.52	190	23.3	
	No Demod.	2.086708	20.41	—	—	—	—	9.3	
10–40	Simple Dem.	2.0867010	33.87	13.46	38.0	0.19	310	13.3	
	EDPV	2.086706	59.70	39.29	38.0	0.59	150	18.6	
	No Demod.	2.086710	24.69	—	—	—	—	14.9	Fig.4 blue
25–70	Simple Dem.	2.086714	31.10	6.41	35.0	0.12	5	17.2	
	EDPV	2.086714	39.18	14.49	38.5	0.56	160	20.1	

[a] : "NoDemod."= th 0th stage, without timing correction; "Simple Dem."= the 1st stage, with corrections using equation (11), and the parameters in the 6th to 8th columns; and " EDPV"= the 2nd stage, with corrections using equation (15) and the parameters in Table 2 .

[b] : Increment in Z_4^2 from the "NoDemod." value.

[c] : The pulsed fraction in percent, of which the errors are given in Fig. 5.

[d] : Cross references within the paper. Fig. 14, Fig. 15, and Fig. 16 apply to all entries (except 8–10 keV) with "EDPV".

[e] : Because of the low energy range, the EDPV corrections have rather small effects.

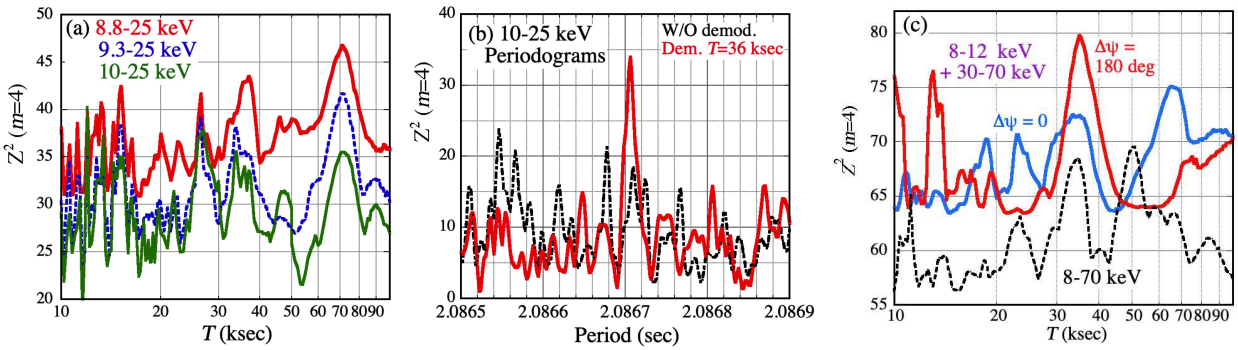

Figure 10. (a) The DeMDs from three energy intervals above 10 keV. From top to bottom, 8.8–25 keV (solid red), 9.3–25 keV (dashed blue), and 10–25 keV (solid green). (b) The 10–25 keV $m = 4$ pulse periodograms, shown on the same period scale as Fig. 3. The dashed black trace is before the demodulation. The solid red trace is after the demodulation, using $A = 0.5$ sec, $\psi = 150°$, and $T = 36.0$ ks. (c) The dashed black trace shows the 8–70 keV DeMD, whereas the blue one uses two disjoint energy intervals, 8–12 keV plus 30–70 keV. The red one is the same, but further incorporating a modulation-phase jump by $\Delta\psi = 180°$ between 12 keV and 30 keV.

haviour of A, in 8–10 keV where the two spectral components have comparable contributions (Fig. 1). The $T = 36$ ks feature has emerged clearly, of which the parameters are summarised in Table 1. Compared to equation (13) describing the 8–25 keV results, $T = 35.0^{+2.1}_{-4.8}$ ks is consistent, $A = 0.12 \pm 0.06$ sec is somewhat smaller, and $\psi = 200° \pm 30°$ could be larger. The 72 ks hump is also seen. The 36 ks phase modulation in this energy band is visualised by a double-folded map in Fig. 8c, which is similar to that in 8–25 keV. The pulse behaviour thus changes at ~ 8 keV, rather than at ~ 12 keV where the HXC and SXC cross over.

4.2.2 Results in > 10 keV

We next examine higher-energy data for the pulsation and its 36 ks phase modulation, trying to solve the puzzle of the reduced PF. With the UD kept at 25 keV as in Fig. 7, we hence raised the LD, from 8 keV to 10 keV stepwise. Figure 10a shows how the DeMD changed in this course. When the LD is raised, *e.g.*, to 8.8 keV, the 36 ks feature became somewhat weaker, whereas the 72 ks hump more prominent. As the LD is further raised to 9.3 keV, the 70 ks hump still remained, but the 36 ks peak nearly disappeared. In addition, the Z_4^2 values on average decreased more than is expected

from the count-rate decrease (by 24% from that in 8–25 keV) via equation (10); this implies a decrease in the PF. These trends further continued to 10–25 keV, where the 36 ks peak became no longer visible.

Thus, some drastic changes in the pulsation is likely to take place as the LD is raised from 8 keV to 10 keV, in such a way that the correction with equation (11), which worked fine for energies 8–25 keV, becomes less effective. Nevertheless, an alternative possibility, that the PF in > 10 keV is intrinsically low, is unlikely, because we keep observing the 72 ks hump, which may be related to the 36 ks feature. Moreover, when $T = 36.0$ ks and $P = P_0$ are fixed, the 9.3–25 keV and 10-25 keV DeMDs yield $\delta Z_4^2 = 13.84$ and $\delta Z_4^2 = 12.63$, respectively, which are not too small. This becomes clear in Fig. 10b, which compares the 10–25 keV periodograms before and after the demodulation. Thus, the correction with equation (11) does enhance the pulsation, but some other values of T give still larger $Z_4^2(P_0)$ as in Fig. 10a (green).

As we suspected in § 3.3.2, these results suggest that the intrinsic PF in the intermediate energy ranges would be in reality much higher than is implied by simple epoch-folding results, and the pulse coherence is degraded by some decoherence processes that cannot be fully described by equation (11). The most likely possibility, as suggested by Fig. 5, is that the pulse behaviour including its 36 ks phase modulation is considerably energy dependent, so the pulses in different energies partially cancel out when the data are accumulated over a wide energy.

The above inference has been reinforced by Fig. 10c. The dashed black trace represents the 8–70 keV DeMD, where the baseline is relatively high at $Z_4^2 \sim 56$ but the 36 ks peak ($Z_4^2 \sim 68$) is not very strong. We then found that the pulse significance generally increases when we discard some intermediate energy intervals. As indicated by a blue curve, this effect became most prominent when the 12–30 keV interval is discarded and the remaining two energy ranges, 8–12 plus 30–70 keV, are used jointly. In spite of a count rate decrease by 40%, on average Z_4^2 became higher, and the 36 ks peak increased to $Z_4^2 = 72.42$. The demodulated PF increased from 15.9% to 21.5 ± 2.9%. Therefore, the suspected decoherence effects are thought to be significant in the excluded 12–30 keV energy range. A surprise was the red DeMD, where the 36 ks peak drastically increased to $Z_4^2 = 79.78$. This curve was obtained in the same manner as the blue one, but assuming that ψ in equation (11) changes by $\Delta\psi = 180°$ between 12 keV and 30 keV. When $\Delta\psi$ is allowed to vary, Z_4^2 became maximum for $\Delta\psi = 170° \pm 50°$. Thus, the decoherence effects are inferred to involve a *phase reversal* in ψ, across the intermediate energy range.

We are here brought back to the issue that has so far been left behind; the energy dependent variations in the pulse phase. To be precise, we need to consider two independent factors. One is the simple energy dependence of the pulse phase, as indicated by Fig. 5 of CZ20 and our Fig. 4. The other is the more complex possibility revealed by Fig. 10c, that ψ in equation (11), and possibly A as well, depend on energy. We call these two mechanisms collectively *energy-dependent pulse variation (EDPV)* effects.

4.3 Energy dependent pulse variation (EDPV)

Assuming that T is energy independent, the idea of EDPV can be formulated by modifying equation (11) as

$$\delta t = P \cdot S(E) + \tilde{A}(E) \sin\left[2\pi t/T - \tilde{\psi}(E)\right] \quad (15)$$

where E is the photon energy in keV, and $S(E)$ ($-1 \le S < 1$, most likely $0 \le S \lesssim 0.25$) describes the energy-dependent but T-unrelated pulse-phase shifts in units of the pulse cycle. The variations depending on both E and the modulation phase Ψ are taken into account by $\tilde{A}(E)$ and $\tilde{\psi}(E)$, which generalise A and ψ in equation (11), respectively. This $\tilde{\psi}(E)$ includes the modulation-phase change by $\Delta\psi$ indicated by Fig. 10c. In a double-folded map, $S(E)$ and $\tilde{\psi}(E)$ respectively represent energy-dependent horizontal and vertical displacements of the pulse pattern; the latter has no meaning when $A = 0$. If we regard Fig. 3 and Fig. 4 as the 0th stage of the pulsation study, the demodulation analysis using equation (11) can be considered as the 1st stage, and the introduction of equation (15) means that we proceed to the 2nd stage.

4.3.1 Formalism

To implement equation (15) into our analysis, we must come up with some appropriate forms of $\tilde{A}(E)$, $\tilde{\psi}(E)$, and $S(E)$, based on the data themselves, as we can invoke neither theoretical predictions, nor past observation of a similar kind. Figure 10 is important, but not yet informative enough. We hence repeated the demodulation analysis in various energy ranges between 8 and 70 keV, chosen to be relatively narrow as long as $Z_4^2(P_0)$ for $T = 36.0$ ks exceeds 25.0. Figure 11a summarises A and ψ that maximize $Z_4^2(P_0)$ at $T = 36.0$ ks. It thus reveals strong energy dependences in both A and ψ; A increases from ~ 0.1 at ~ 10 keV, to ~ 0.5 at $E \sim 20$ keV, and then returns to ~ 0.1 at $E > 30$ keV. These variations in A naturally explain why the pulse significance increased in Fig. 10c by excluding the 12–30 keV interval.

As indicated by yellow diamonds in Fig. 11a, ψ starts from $\sim 180°$, and gradually decreases towards higher energies up to ~ 30 keV, but the drop meantime is only $\sim 60°$. In particular, the change from 12 keV to 30 keV is only $\sim 20°$, much smaller than $\Delta\psi \sim 180°$ suggested by Fig. 10c. Instead, as shown by a purple diamond, the 27–70 keV data point implies a sudden change in ψ: it was in reality obtained at $\psi = 340° \pm 25°$, but for the presentation, it is shown after shifting by $180°$ along the ordinate. Since this result is likely to reflect the reversal in $\tilde{\psi}$, we returned to Fig. 10c and changed the upper bound E_3 of the excluded energy region. As E_3 was gradually lowered from 30 keV, the optimum $\Delta\psi$ remained at $150° - 180°$, until $E_3 \lesssim 25$ keV when the advantage of assuming $\Delta\psi \neq 0$ quickly diminished. Considering these, we may regard $\tilde{\psi}(E)$ as gradually decreasing from $E \sim 10$ keV to ~ 25 keV, followed by a $\sim 180°$ jump (phase reversal) in the narrow 25–30 keV interval.

Just for a cross confirmation, panels (d)– (f) of Fig. 8 show double-folded maps in three energy bands above 10 keV. Like in panels (b) and (c), the 10–12 keV map in (d) again shows a wiggling ridge, starting from $(\Phi/2\pi, \Psi/2\pi) \sim (1.1, 0.2)$ to run down to $(1.3, 0.9)$. A difference from the 8–10 keV map is a feature at $(\Phi/2\pi, \Psi/2\pi) \sim (1.4, 0.2)$, which may have disturbed the simple demodulation. Panel (e) in 12–25 keV is

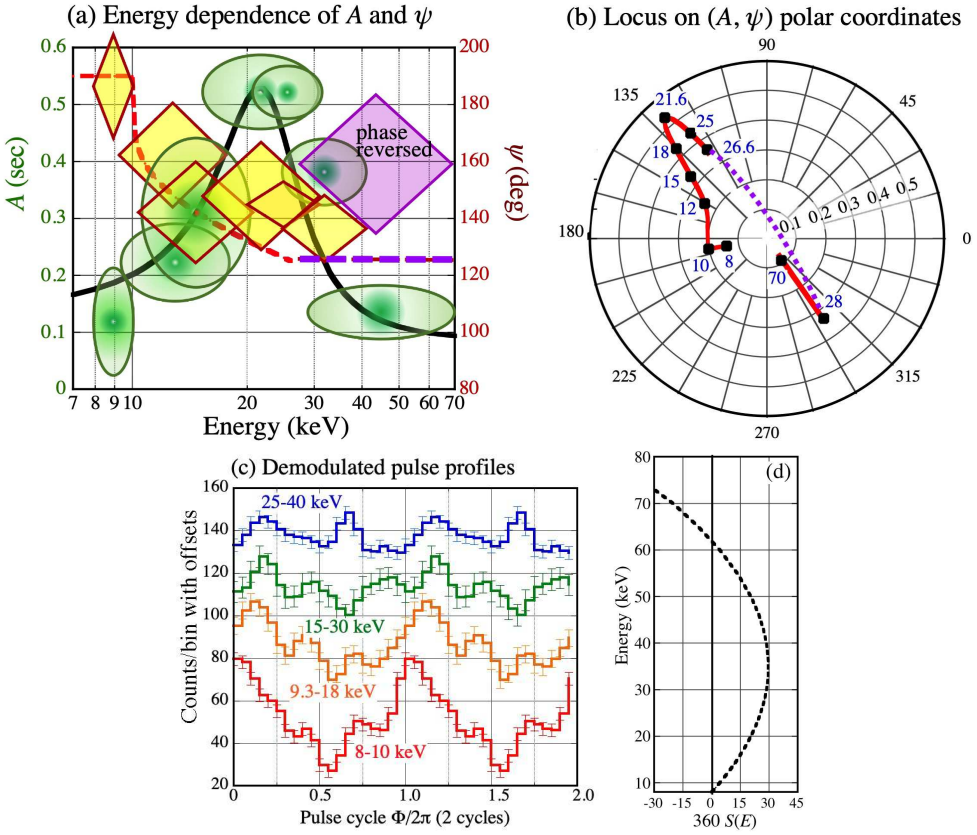

Figure 11. (a) The values of A (green ellipses) and ψ (yellow diamonds) that maximize Z_4^2 at $T = 36.0$ ks (fixed) and $P \sim P_0$, calculated in various energy bands. The vertical heights of these symbols represent $\pm 1\sigma$ errors, and their lateral widths the employed energy ranges. The 27–70 keV $\tilde{\psi}$ data point (purple diamond) is shown by adding 180°. The thick black curve and the dashed red line describe $\tilde{A}(E)$ and $\tilde{\psi}(E)$, respectively, using the optimum parameters in Table 2. At $\geq$ 26.6 keV, $\tilde{\psi}(E)$ makes a 180° phase flip as indicated by the dashed purple line. (b) Locus of the best-estimated $\tilde{A}(E)$ and $\tilde{\psi}(E)$, shown on the (A, ψ) polar coordinates. The numbers in blue are the energy in keV. The dotted purple line indicates a possible trajectory across the ψ reversal. (c) Pulse profiles in several energy bands used in panel (a), shown again with the running average, and vertical offsets to avoid overlap. They were obtained through the demodulation using $T = 36.0$ ks, and the optimum A and ψ determined in respective bands. (d) The form of $S(E)$ in equation (18), calculated using the parameters in Table 2 and shown in unit of degree, after multiplication by 360°. The energy E is taken as the ordinate.

more complex and ambiguous, but one of possible interpretations could be that the pulse ridge leads from $(0.9, 0.2)$ to $(1.2, 0.9)$, with a larger lateral swing as suggested by Fig. 11a, and another wiggling feature runs roughly in parallel, from $(1.3, 0.1)$ to $(1.6, 0.7)$. In the 25–70 keV map, which is also rather noisy, the main ridge may have returned more straight at $\Phi/2\pi \sim 1.2$, which is somewhat delayed, as represented by $S(E)$, from those in 3–8 keV. Furthermore, the ridge could be most advanced at $\Psi/2\pi \sim 0.6$, which is opposite to the behaviour in panels (b) and (c). This is consistent with the phase reversal in $\tilde{\psi}(E)$ at ~ 25 keV. Thus, the double-folded maps, though not quantitative, appear generally consistent with Fig. 11.

From these preparations, $\tilde{A}(E)$ may be regarded as consisting of a constant floor at $A \sim 0.1$, plus a sharp enhancement centred at ~ 20 keV which has a height of $A \sim 0.5$ and a width of ~ 10 keV. As a simple analytic form to empirically describe such a profile, we choose a Lorentzian plus a constant, and describe as

$$\tilde{A}'(E) = A_0 \left[a_{\rm f} + \frac{1 - a_{\rm f}}{1.0 + \{(E - E_{\rm c})/E_{\rm w}\}^2} \right] . \qquad (16)$$

using three parameters; the centroid $E_{\rm c}$ and the width $E_{\rm c}$ of the Lorentzian, and a dimensionless amplitude floor $a_{\rm f}$. In addition, A_0 replaces A in equation (11). As superposed in Fig. 11a on the data, $\tilde{A}(E)$ reaches the maximum of A_0 at $E = E_{\rm c}$, and decreases at $E > E_{\rm c}$ to approach $A_0 a_{\rm f}$.

Based on the considerations performed so far, $\tilde{\psi}(E)$ is modeled as as

$$\tilde{\psi}(E) = \begin{cases} \psi_0 & (E \leq 10) \\ \psi_0 - \psi_{\rm d}\,[(E-10)/(E_{\rm d}-10)]^{\gamma} & (10 < E < E_{\rm d}) \\ \psi_0 - (\psi_{\rm d} + \Delta\psi) & (E_{\rm d} < E) \end{cases} \qquad (17)$$

using five parameters, ψ_0, $\psi_{\rm d}$, $E_{\rm d}$, γ, and $\Delta\psi$. Here, ψ_0 replaces ψ in equation (11), and specifies the initial modulation phase at $E \leq 10$ keV. From $E = 10$ keV to $E = E_{\rm d} \sim 25$ keV, $\tilde{\psi}$ is assumed to decrease by $\psi_{\rm d}$, as a power-law function of E with an index $\gamma > 0$. At $E = E_{\rm d}$, $\tilde{\psi}$ reaches $\psi_0 - \psi_{\rm d}$ where it makes the phase jump by $\Delta\psi \sim 180°$, and stays there afterwards. Assuming no energy dependence after the phase jump is justified by the constancy of $\Delta\psi$ when we scanned E_3 from 30 keV to 25 keV. The functional form of $\tilde{\psi}$ is also superposed in Fig. 11a on the data, where the purple portion is subject to the phase reversal.

To get an idea on $S(E)$, we show in Fig. 11c the pulse profiles folded at P_0, in four representative (and slightly overlapping) energy bands chosen from those used in panel (a). Unlike Fig. 4, these profiles have been derived through demodulation, using equation (11) assuming $T = 36.0$ ks, together with the optimizing A and ψ in each energy band. Here, the simple demodulation has already made the pulse profiles behave much more systematically as a function of energy than before. Among the lower 3 bands, the main pulse peak and the pulse minimum are both seen to shift positively as a function of energy, whereas the dependence appears to saturate (except the sub peak in 25–40 keV emerging at $\Phi/2\pi \sim 0.6$) when the highest two bands are compared. Therefore, we have chosen to express $S(E)$ using a simple parabolic function as

$$S(E) = \frac{R/360}{(E_{\rm piv} - 8)}(E - 8)(E_{\rm piv} - E) \qquad (18)$$

for $E > 8$ keV and $S(E) = 0$ for $E < 8$ keV, with two free parameters; the pivot energy $E_{\rm piv}$ where the modulation phase returns to that at 8 keV, and the rate of the pulse-phase change at 8.0 keV, $R \equiv \{dS(E)/dE\}_{\rm 8keV}$ in units of degree per keV. The pulse-phase lag increases for $8 < E < (8 + E_{\rm piv})/2$, decreases for $(8 + E_{\rm piv})/2 < E < E_{\rm piv}$, and turns negative for $E > E_{\rm piv}$. This function is illustrated in Fig. 11d, where we rotated the coordinate direction so as to simulate panel (c). The result does not change very much, if the start point is set at 10 keV instead of 8 keV.

4.3.2 Optimisation of the new parameters

The above 2nd-stage recipe with equations (15) through (18) altogether involves 9 new parameters, $E_{\rm c}$, $E_{\rm w}$, $a_{\rm f}$, $\psi_{\rm d}$, $E_{\rm d}$, γ, $\Delta\psi$, R, and $E_{\rm piv}$, in addition to A_0 and ψ_0. The 9 new parameters, once appropriately optimized, are expected to significantly enhance the $T = 36$ ks peak in the DeMDs at any energy, using a common pair of (A_0, ψ_0). To achieve this goal, we have selected an intermediate energy band of 10–40 keV, because $\tilde{A}(E)$, $\tilde{\psi}(E)$, and $S(E)$ are all inferred to be most energy dependent around these energies, and the photon statistics are still sufficient. Some pilot studies indicated that the data still prefer $\Delta\psi \sim 180^\circ$ within a tolerance of $\pm 30^\circ$, and a rather small index as $\gamma = 0.2-0.3$. We hereafter assume $\Delta\psi = 180^\circ$ and $\gamma = 0.25$ both fixed, and try to optimize the remaining 7 parameters.

We have hence trimmed $E_{\rm c}$, $E_{\rm w}$, $a_{\rm f}$, $\psi_{\rm d}$, $E_{\rm d}$, R, and $E_{\rm piv}$, in addition to A_0 and ψ_0, so as to maximize Z_4^2 in the 10–40 keV interval for $T \sim 36.0$ ks and $P \sim P_0$. Then, their optimum values and typical errors have been determined as in Table 2. The functional forms of $\tilde{A}(E)$ and $\tilde{\psi}(E)$, plotted in Fig. 11a, actually employ these optimum parameters. They are seen to approximately reproduce the data behaviour, although the best-estimated $\tilde{\psi}(E)$ decreases with energy somewhat less steeply than the yellow diamonds. Also, the $S(E)$ curve in Fig. 11d is drawn using these optimum values of R and $E_{\rm piv}$. Thus, the HXC pulse phase is implied to vary with energy by ~ 0.08 pulse cycles (CZ20), independently of the 36 ks modulation phase.

Figure 11b shows the locus of the best-estimated $\tilde{A}(E)$ and $\tilde{\psi}(E)$, on the (A, ψ) polar coordinate. As indicated with the dashed purple line, the phase reversal is understood as a quick motion of the data point through $A \sim 0$, even though the exact locus of the phase reversal is unconstrained.

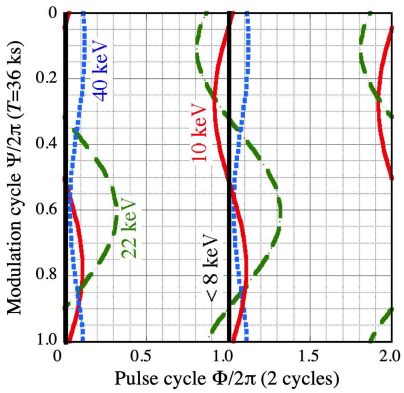

Figure 12. Loci of the pulse peaks indicated by equations (15) – (18) and the parameters in Table 2, shown on the same two-dimensional plane as Fig. 8. Black, red, dashed green, and dotted blue are the predictions for < 8 keV, 10 keV, 22 keV, and 40 keV, respectively, to compare with panels (a), (c), (e), and (f) of Fig. 8.

4.3.3 Results

Figure 12 depicts the pulse-peak behaviour at four representative energies, as specified by the optimum EDPV parameters (Table 2). The plot utilises the same coordinates as Fig. 8, where energy-dependent vertical and horizontal shifts of the pulse-peak loci are represented by $\tilde{\psi}(E)$ and $S(E)$, respectively. The straight black lines represent the pulses at $E < 8$ keV, as in Fig. 8a. The red curve for $E = 10$ keV is similar to the wiggling pulse-peak locus in Fig. 8c, and the green curve for $E = 22$ keV $\approx E_{\rm c}$ is seen to crudely emulate our particular interpretation of Fig. 8e (although the secondary feature is not reproduced here). Reflecting the decrease in $\tilde{\psi}$ from 10 to 22 keV by about 60° (Fig. 11a), the green curve is shifted upwards by ~ 0.2 cycles compared to the red one. The blue curve, to be compared with Fig. 8f, has the opposite modulation phase compared to the green curve, because of the phase reversal at $E \sim 27$ keV.

Below, we adopt the formalism using equations (15) through (18), and the parameters in Table 2, as the final solution of our 2nd-stage study.

Figure 13 shows double-folded maps produced after correcting the arrival times of all photons for the EDPV effects, using the final solution in Table 2. Compared with the 0th-stage results in Fig. 8, the 8–25 keV map shows a more straight ridge. Although this is simply the 1st-stage effect, the benefit of the 2nd-stage corrections emerges in the two higher-energy maps, where the main pulse peak appears at a constant pulse phase of $\Phi/2\pi \sim 1.0$, like in 8–25 keV. In addition, the 12–25 keV map reveals two sub-pulse loci which are also rather straight. Thus, Fig. 13 illustrates what can, and what cannot, be achieved in the 2nd stage. Namely, our EDPV corrections apply an energy dependent horizontal displacement to each row of the map, to make the pulse ridge(s) vertically as straight as possible. In contrast, details of the Ψ-dependent variations in the pulse profiles cannot be fixed by this method.

For more quantitative evaluations of the EDPV corrections, we conducted a series of studies using the following four energy intervals; (a) the overall 8–70 keV band, (b) the 8–25 keV range where the analysis started, (c) the 10–40 keV band where he EDPV parameters are optimized, and (d) 25–

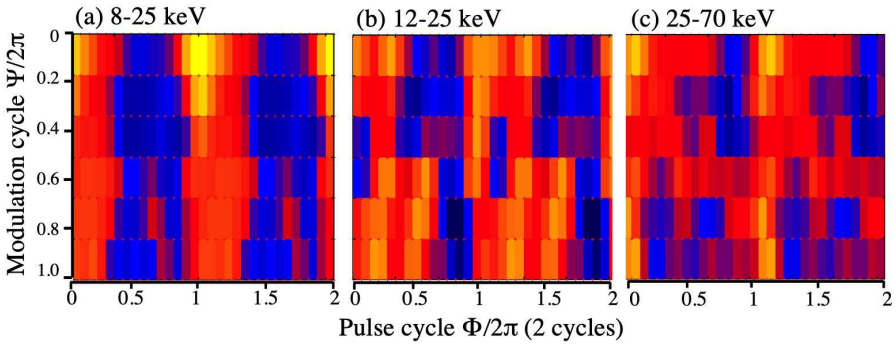

Figure 13. The double-folded maps obtained after correcting all the photon arrival times using the EDPV parameters in Table 2, together with $A_0 = 0.52$ s, $\psi_0 = 190°$, and $T = 36$ ks. Panels (a), (b), and (c) should be compared with panels (b), (e), and (f) in Fig. 8, respectively.

Table 2. The EDPV parameters optimized in 10–40 keV.

Parameter	Eq. (15)(16)		Eq. (19)	Eq. (20)[c]
	value	error[a]	value	value
$\tilde{A}(E)$				
E_c (keV)	21.6	0.4	20.5	21.1
E_w (keV)	6.9	0.3	8.5	3.6
a_f	0.16	0.03	0.16	0.18
$\tilde{\psi}(E)$				
ψ_d (deg)	66.5	2.5	69.0	64.0
E_d (keV)	26.6	0.8	26.7	26.6
γ [b]	(0.25)	—	(0.25)	(0.25)
$\Delta\psi$ (deg) [b]	(180)	—	(180)	(180)
$S(E)$				
R (deg/keV)	2.2	0.5	3.2	2.6
E_{piv} (keV)	62	15	72	76
T (ks)	38.0	2.0	38.0	37.0
A_0 (sec)	0.59	0.03	0.47	0.46
ψ_0 (deg)	150	20	150	150
Z_4^2	59.70	–	59.57	62.47

[a] : These errors apply to equations (16), (19), and (20).

[b] : Fixed base on some pilot studies.

[c] : With $\sigma = 30$ fixed.

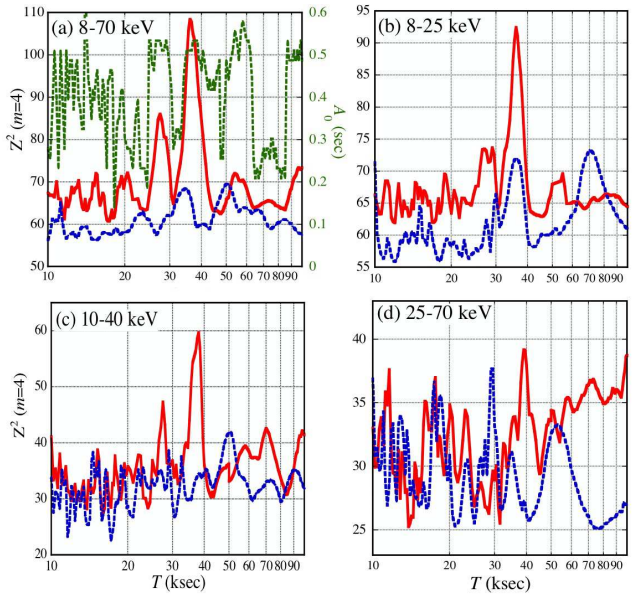

Figure 14. The $m = 4$ DeMDs in the four energy intervals. Solid red lines indicate the results obtained in the 2nd stage (*i.e.*, the EDPV corrections), using the parameters in Table 2. Dashed blue curves show the 1st-stage results, *i.e.*, the simple demodulation using equation (11); the blue one in (b) is identical to the $m = 4$ result in Fig. 7. In (a), the behaviour of A_0 in the 2nd stage is shown in green. See text for further details.

70 keV to test the recipe against the hardest photons. These energy ranges mutually overlap, and none of (a), (b), or (d) is disjoint from (c) which was used for the parameter optimisation. The derived results are presented in Fig. 14, Fig. 15, and Fig. 16, where panels (a) through (d) represent the four energy bands, respectively. The EDPV parameters were all fixed throughout to those in Table 2, and $m = 4$ was retained as before.

Figure 14 presents the DeMDs derived in the 2nd stage (solid red), in comparison with those from the 1st-stage analysis (dashed blue). As T is varied, both A_0 and ψ_0 (or A and ψ) were allowed to vary, and P to change over the error range of equation (7). Figure 15 compares the pulse periodograms in each energy range, derived under three conditions; without demodulation (0th stage; dashed black), with the energy-independent demodulation (1st stage; solid blue), and incorporating the EDPV corrections (2nd stage; solid red). The red and blue curves were computed using the parameters at the $T \sim 36$ ks peak in Fig. 14, and the associated values of A_0 and ψ_0 (or A and ψ). The parameters of these periodogram peaks are summarised in Table 1, separately for the 3 conditions. Finally, Fig. 16 presents the folded pulse profiles, derived under the same 3 conditions. Figure 16e compiles the finally derived 4 pulse profiles, and the 6-8 keV one from the simple folding.

The three figures reveal impacts of the EDPV corrections, which can be summarised in the following points.

(i) In Fig. 14, the 36 ks peak appeared strongly in all 2nd-stage DeMDs, particularly in (a) through (c), and the $T \sim 72$ ks peak disappeared in (b). Even in (d), the peak appears at $T = 39.0$ ks, which is still within 1.3 sigmas of equation (13).

(ii) The values of T via the EDMP corrections (Table 1) are generally consistent with equation (13), and the *Suzaku*

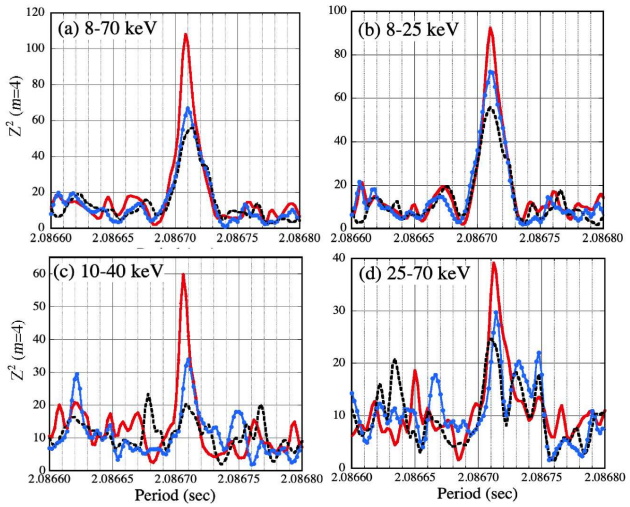

Figure 15. The pulse periodograms in the four energy ranges. The meanings of the red and blue curves are the same as in Fig. 14, wheres the dashed black lines represent the results without any demodulation correction (0th stage).

measurement in equation (4). The periodogram peak remains at P_0 of equation (7) within the error. Furthermore, $A_0 \sim 0.52$ sec and $\psi_0 = 180° \pm 30°$ obtained in the 2nd stage (Table 1) are both relatively energy independent.

(iii) In all the four energy bands, the EDPV corrections increased the pulse significance by $\delta Z_4^2 > 8$, compared to those from the 1st stages (Table 1). In 8–70 keV, *e.g.*, the increase from $Z_4^2 = 68.43$ (1st stage) to 108.38 (2nd) by $\delta Z_4^2 = 39.95$ means an 8-orders-of-magnitude decrease in the pre-trial probability (Appendix A), even though that in the post-trial probability is not obvious because we must consider the number of independent trials in optimizing the 7+2 EDPV parameters. (This cannot be easily Monte-Carlo evaluated, as the parameter scanning demands huge computational times.)

(iv) In response to the increase in Z_4^2 (equation 10), the PF increased to $\gtrsim 18\%$ in all energies (Table 1). Even though these are still lower than measured in < 8 keV, the puzzle with Fig. 5 has been solved at least partially.

(v) Figure 16e provides the most impressive result of the present study, where the pulse profiles have become very similar and in-phase to one another, with a sharp rise and a slow decline. The main peak is at $\Phi/2\pi \sim 0.1$, and two sub-peaks are seen at $\Phi/2\pi \sim 0.4$ and ~ 0.7. The separations among these peaks, 1/4–1/3 pulse cycles, justify our use of $m = 4$. These features sharpen towards higher energies; so does the periodogram peak. In contrast to the irregular energy dependence in Fig. 4, the regular pulse profiles revealed here highlight the achievements in the 2nd stage.

Of course, these results might be trivial for the 10–40 keV interval (panels c), because the EDPV parameters have been optimized to enhance the pulse visibility there. To remove this concern, we conducted the same parameter optimisation (except $\Delta\psi$ and γ which are fixed) using the other three energy ranges. Then, in any of them, the optimum values of the 7 parameters became consistent, within errors, with those determined in 10–40 keV (Table 2). Equivalently, in none of (a), (b), or (d), the parameter re-adjustment increased Z_4^2 by more than ~ 2, above that ("EDPV" row in Table 1) specified by the parameters determined in 10–40 keV. In particular, the agreement between the two disjoint intervals, 8–25 keV and 25–70 keV, is assuring.

In closing this section, we may examine how the three energy-dependent functions contribute individually to the Z_4^2 increment. Although the answer depends on the energy, generally replacing A to $\tilde{A}(E)$ is most effective, contributing about half of δZ_4^2 above the case of simple demodulation. Then, the remaining half is contributed about equally by $\tilde{\psi}(E)$ and $S(E)$. The three corrections are all mandatory.

5 DISCUSSION

5.1 Summary of the obtained results

We analysed the *NuSTAR* data of 1E 1547−5408 acquired on 2016 August 23 to 24, mainly focusing on its pulsation detected at the period of equation (7). As reported by CZ20 who already analysed the same data, the PF decreased markedly in the intermediate energy range (Fig. 5), and the folded pulse profiles exhibited complicated energy dependences (Fig. 4). Using these puzzles as a springboard, we carried out further timing analysis in two stages.

In the 1st stage, we conducted the demodulation analysis, employing equation (11) and assuming that A and ψ are both constant over the data-accumulation energy range. In < 8 keV where the SXC dominates, the pulse was free from phase modulation, like in the *Suzaku* data. In the 8–25 keV band, we reconfirmed the 36 ks pulse-phase modulation (Fig. 7) discovered with *Suzaku*. The detection of this effect both in an outburst and quiescence suggests that it is a persistent phenomenon, presumably due to celestial mechanics, rather than a transient episode in a high activity. This phenomenon is also regarded as rather common to magnetars, because it has been confirmed in two contrasting sources, 1E 1547−5408 with the fastest rotation and high variability, and 4U 0142+61 which is relatively persistent and has two orders of magnitude larger characteristic age. We hence follow Paper I, and interpret the 36 ks periodicity as the slip period associated with free precession of the NS, which is axially deformed to $\epsilon \sim 0.6 \times 10^{-4}$.

In > 10 keV, in contrast, the demodulation was effective only to a limited degree; the DeMDs did not show noticeable peaks at $T \sim 36$ ks (Fig. 10a), and the puzzles have remained unsolved. Through detailed inspections of the data (Fig. 10b, c), we recognized that the problem stems from the strong energy dependence (EDPV) of the HXC pulse properties, and carried out the 2nd-stage analysis, for the first time in our studies of this subject. That is, guided by the inspections and further data analysis (Fig. 11), we modeled the EDPV effects by the three empirical functions, $\tilde{A}(E)$, $\tilde{\psi}(E)$, and $S(E)$. By optimizing their parameters in the 10–40 keV range, and using the results to correct the photon arrival times in energy-dependent ways (Fig. 12), the 36 ks peak in the DeMDs have been restored, from 10 keV to 70 keV (Fig. 14). This establishes that the 36 ks pulse-phase modulation is an intrinsic property of the HXC of this object. The corrections have also solved the puzzling behaviour of the HXC pulses; the PF has increased to $\gtrsim 18\%$, and the irregular energy dependence of the pulse profiles has been rectified (Fig. 16).

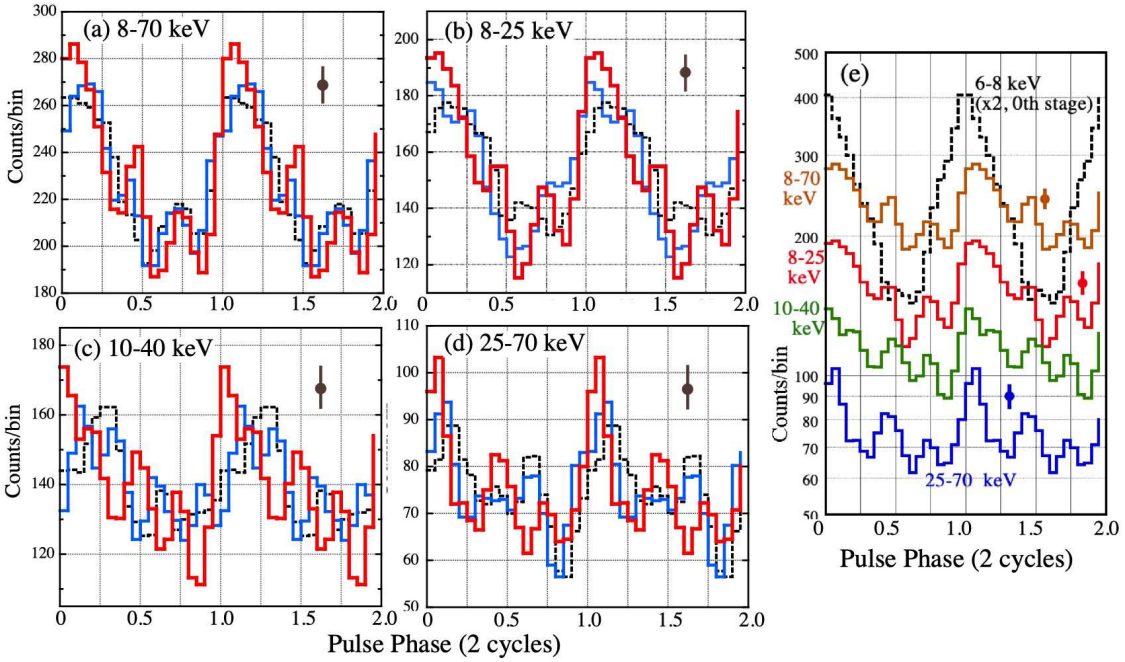

Figure 16. (a) to (d): Pulse profiles in the four energy ranges, folded using the parameters at the peak of the corresponding periodogram in Fig. 15. The meanings of the solid red, solid blue, and dashed black lines are the same as in Fig. 15. (e) A compilation of the red profiles in panels (a) through (d), shown together using a logarithmic ordinate. The 10-40 keV profile was scaled by 0.8 just to avoid overlap. The dotted black curve shows the 6-8 keV profile (doubled for presentation), obtained with no demodulation.

In several places, we used the running average. As describe in Appendix B, this process suppresses noise with high spatial frequencies, to make the pulse profiles and double-folded maps easier to grasp. Although it also affects the data statistics, the major quantitative evaluations of the present work remain intact, because they are all based on the Z^2_n method that incorporates no running average.

Below, we examine these 2nd-stage results from three aspects; appropriateness of this EDPV modeling, geometrical scenarios in terms of the free precession, and possible astrophysical interpretations.

5.2 Reality of the EDPV modeling

Our EDPV modeling is apparently supported by the two results described in § 4.3.3; the different portions of the 8–70 keV energy band yielded consistent EDPV parameters, and the pulse phase has become highly coherent as a function of energy (Fig. 16e). Nevertheless, the modeling is admittedly very extraordinary; equation (16) claims that A is enhanced at ~ 22 keV, almost like a resonance, to reach $\sim \pm 1/4$ of a pulse cycle. The phase reversal in Ψ was also rather unexpected. In addition, the data in Fig. 11a are subject to large errors. Yet another concern is that the several characteristic energies (*e.g.*, 8, 10, 21.6, and 26.6 keV) involved in our modeling are apparently not accompanied by any noticeable spectral features (Fig. 1; Fig. 2 of CZ20). Therefore, we should carefully evaluate the reality of this picture, and examine other possible modelings.

Although the data points in Fig. 11a suggest smooth variations of A, this can be an artifact due to the use of overlapping data points. The truth might be that A jumps abruptly, at some energies, between $A \sim 0.1$ and ~ 0.5. We can emulate such a case by modifying equation (16) as

$$\tilde{A}'(E) = A_0 \left[a_{\rm f} + \frac{1 - a_{\rm f}}{1.0 + \{(E - E_{\rm c})/E_{\rm w}\}^4} \right] \ . \qquad (19)$$

Here, the 4th power expresses more rapid changes than the original Lorentzian, using the same three parameters as before. This $\tilde{A}'(E)$, together with the same $\tilde{\psi}(E)$ and $S(E)$ as before, were substituted into equation (15), and again all parameters of $\tilde{A}'(E)$, $\tilde{\psi}(E)$, and $S(E)$ were optimized. The results are summarised in Table 2, and the profile of the optimum $\tilde{A}'(E)$ is drawn in Fig. 17 in comparison with the original $\tilde{A}(E)$. Indeed, $\tilde{A}'(E)$ emulates a transition-like behaviour between $A \sim 0.1$ and $A \sim 0.45$, and reconfirms the marked increase of A at ~ 20 keV. However, the maximum Z^2_4 thus achieved was lower by 0.13, than that obtained with equation (16). Furthermore, when the parameters are optimized in the 8–70 keV range, $\tilde{A}'(E)$ again gave a value of Z^2_4 which is lower by 3.75 than $\tilde{A}(E)$. Therefore, we do not find a good reason to replace $\tilde{A}(E)$ with $\tilde{A}'(E)$.

Returning to the original Lorentzian form, the model-implied value of A at $E \sim E_{\rm c}$ is similar to that found with *Suzaku* (Paper I), $A = 0.52 \pm 0.14$ sec (although in that case A was not strongly energy dependent at $E \gtrsim 10$ keV). Such a large A could arise (Paper I) if the pulse profile comprises two peaks separated by about half a pulse cycle, and their relative intensities interchange through the 36 ks phase. If so, we expect the pulse peak to draw a square-wave like locus on the double-folded map, rather than the sinusoidal variation assumed so far. Actually, in Fig. 8e, the 12–25 keV pulse peak appears to keep a rather constant phase over $\Psi/2\pi = 0 - 0.5$, and then jumps to a different phase over $\Psi/2\pi = 0.5 - 1.0$. Introducing another parameter $\sigma \geq 0$, we hence modified the

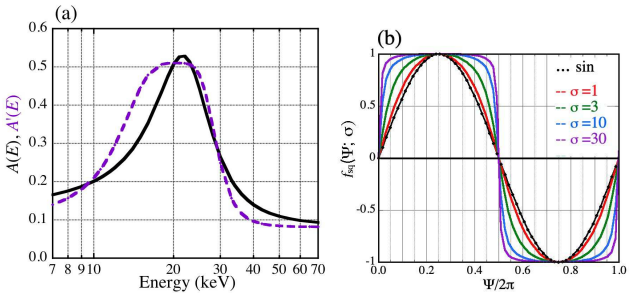

Figure 17. (a) The behaviour of $\tilde{A}'(E)$ (equation 19) in dashed purple, compared with that of $\tilde{A}(E)$ (equation 16) in solid black. Both have been optimized in the 10–40 keV range. The corresponding parameters are given in Table 2. (b) The square-wave-like modulation profiles $f_{\rm sq}(\Psi;\sigma)$ specified by equation (20), shown against $\Psi/2\pi$ for different values of σ.

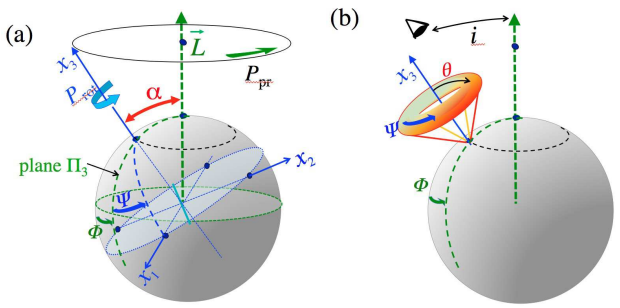

Figure 18. (a) The assumed geometry of the object, where the observer and the star's centre are on the plane of the sheet. (b) The assumed conical beam pattern of the HXC, where the azimuthal variation of the emissivity is indicated by colors.

$\sin(\Psi)$ factor (for simplicity $\tilde{\psi}$ was set 0) in equation (15) to (Makishima et al. 2016)

$$f_{\rm sq}(\Psi;\sigma) \equiv \frac{\arctan\{\sigma\sin(\Psi)\}}{\arctan(\sigma)} \ , \qquad (20)$$

which reduces to $\sin(\Psi)$ if $\sigma \ll 1$. As shown in Fig. 17b, $f_{\rm sq}(\Psi;\sigma)$ becomes saturated as σ increases, and approaches a square wave that oscillates between ±1 with 50% duty ratio. Replacing $\sin(\Psi)$ in equation (15) with $f_{\rm sq}(\Psi;\sigma)$, we repeated the 2nd-stage analysis of the 10–40 keV data. As σ is changed, all the other model parameters were re-optimized. Then, as in the last column of Table 2, Z_4^2 increased by 2.77 for $\sigma \sim 30$ (with a typical uncertainty of ±20) over the sinusoidal case ($\sigma \to 0$). When selecting the 8–70 keV range instead, the case with $\sigma \sim 30$ was again favored, as Z_4^2 was larger by ~ 2.0. Therefore, as suggested by Fig. 8e, the actual phase-modulation waveform could be fairly square-wave like, rather than sinusoidal. However, the data preference for $f_{\rm sq}(\Psi;\sigma)$ than $\sin(\Psi)$ may not be obvious statistically, because the introduction of σ means an additional increase in the number of trials.

From these evaluations, we conclude that the functional forms of $\tilde{A}(E)$, $\tilde{\psi}(E)$, and $S(E)$, expressed by equations (16), (17), and (18) respectively, provide a reasonable account of the pulse-phase behaviour above 8 keV, although the modulation waveform as a function of Ψ may deviate somewhat from sinusoidal to become square-wave like. In any case, these results must be regarded as tentative, possibly with considerable room for future improvements.

5.3 Possible emission geometry

We next consider geometrical models that can explain the observed pulse-phase behaviour, in the framework that the 36 ks period represents the slip period T of equation (2), associated with the free precession of the NS. Below, we refer to Fig. 18a, which utilises the nomenclature introduced in § 1. Here, $\hat{x}_3$ is identified with the stellar dipole-field axis, Π_3 denotes the plane defined by $\hat{x}_3$ and $\vec{L}$, and the observer's line of sight lies on the plane of the sheet. Our basic assumption is that the HXC emissivity pattern is energy dependent, but not time dependent if expressed in the $(\hat{x}_1, \hat{x}_2, \hat{x}_3)$ frame which is fixed to the NS: the observed time variability is solely due to the motion of the stellar frame, relative to the inertial frame where the observer is located.

With this setup, the basic idea to explain the periodic pulse-phase modulation in a magnetar is to invoke three levels of symmetry breaking (§ 1; Paper I; Makishima et al. (2014, 2019)); (i) $\alpha \neq 0$, as evidenced by the clear pulsation; (ii) $\epsilon \neq 0$, *i.e.*, the NS is aspherical (but axially symmetric); and (iii) the HXC emission pattern is asymmetric around $\hat{x}_3$. According to (i), Π_3 rotates around $\vec{L}$ with the period $P_{\rm pr}$, and its rotation phase relative to the observer's line of sight is identified with the pulse phase Φ of equation (8). When (ii) holds as well, the NS also rotates around $\hat{x}_3$ *relative to* Π_3, with the slip period T. The angle of this rotation seen from Π_3 coincides with the modulation phase Ψ defined by equation (12). The triplet (Φ, α, Ψ) serves as the three Euler angles that transform the observer's frame to $(\hat{x}_1, \hat{x}_2, \hat{x}_3)$. On a double-folded map drawn on the $(\Phi/2\pi, \Psi/2\pi)$ plane, the X-ray intensity depends on Φ, and also becomes dependent on Ψ when the condition (iii) sets in (*e.g.*, Fig. 8b).

The condition (iii) is fulfilled (Makishima et al. 2014) if the emission region is displaced from $\hat{x}_3$ on the NS surface, or the beaming direction is tilted from $\hat{x}_3$. Here, we employ the latter case, and assume, with some modifications over the toy model of Makishima et al. (2019), that the emission has a conical beam pattern around $\hat{x}_3$ as illustrated in Fig. 18b. The cone is assumed to be geometrically symmetric around $\hat{x}_3$, with a half opening angle θ, and emit hard X-rays along its generatrices, with a full-width-at-half-maximum divergence angle of $\pm45^\circ$ as measured from the cone surface. The case with $\theta \to 0$ reduces to the pencil-beam configuration aligned with $\hat{x}_3$, whereas $\theta \to 90^\circ$ represents the fan-beam configuration as assumed in Fig.12 of Paper I to explain the *Suzaku* result. Moreover, the cone is assumed to be physically asymmetric, so that its directional emissivity depends on the cone's azimuth (the color gradient in Fig. 18b) as $\propto \left[1 + a\cos\left\{\Psi - \tilde{\psi}(E)\right\}\right]$, where a $(0 \leq 1 \leq 1)$ specifies the degree of asymmetry around $\hat{x}_3$. The condition (iii) requires both $\theta > 0$ and $a > 0$.

Figure 19 shows the pulse-phase behaviour, predicted by the above toy model for several representative values of θ. We assumed a viewing inclination angle $i = 40^\circ$ to $\vec{L}$, and $\alpha = 45^\circ$ to avoid self-occultation effects. In addition, we assumed $a = 0.5$ (a mild asymmetry), and $\tilde{\psi} = 170^\circ$ ignoring its complex energy dependence. The emission from the other

pole was neglected, as well as general relativistic light bending effects. The calculated modulation amplitude thus increases as θ gets larger, up to $A \sim \pm P_0/4$ at $\theta \gtrsim 50^\circ$. Therefore, the behaviour of $\tilde{A}(E)$ can be explained if θ somehow increases to $\theta \sim 50^\circ$ at $E \sim 22$ keV. In particular, Fig. 19d looks rather similar to Fig. 8e. Panel (e) with $\theta = 60^\circ$ may apply to the *Suzaku* result, wherein two comparable pulse peaks (from the same magnetic pole), half a cycle apart, interchanged in intensity as a function of Ψ (Fig. 2b of Paper I). Another effect of increasing θ is that the modulation waveform gets gradually deviated from a sinusoidal shape, and becomes square-wave like; this may agree with the data preference for equation (20) (Table 2 last column).

The above toy model thus works at least to a crude approximation, but the results should be taken with several reservations. First, Fig. 19 is meant to show that some emission geometry can roughly explain the present observation, rather than to claim that the selected model or the geometrical parameters are correct. Second, the behaviour of $\tilde{\psi}(E)$ would also be incorporated into Fig. 19, although the present calculation took into account neither this adjustment, nor the ~ 27 keV reversal in Ψ. Third, a similar sequence as changing θ can be obtained by fixing $\theta \sim 50^\circ$, and instead increasing a from 0 to 0.5. Fourth, the behaviour of $S(E)$ is more difficult, than those of $\tilde{A}(E)$ and $\tilde{\psi}(E)$, to reproduce by this model, and probably we need to incorporate also energy-dependent displacements in the emission region. Lastly, Fig. 19 predicts that the Φ-averaged X-ray intensity depends on Ψ. Such a behaviour is seen in Fig. 8, although it is not obvious whether it matches the calculation.

Evidently, a more advanced data analysis would be to compare numerically the observational data as in Fig. 8, with the geometrical predictions as in Fig. 19. This would enable us to see whether the model can quantitatively reproduce the observation, and if so, to constrain the geometrical parameters, α, i, $\theta(E)$, and $a(E)$, as well as $\tilde{\psi}(E)$. This attempt will be our future study.

5.4 Astrophysical interpretations

The final step of the present study is to seek for possible astrophysical interpretations of the obtained results, including the geometrical model constructed in § 5.3. The attempt will be very crude and speculative, because the hard X-ray emission mechanism of magnetars itself is still unknown, and the above geometrical model could be one of many possibilities. Below, we consider six specific queries; [Q1] does the assumed conical emission pattern have any astrophysical basis; [Q2] how the asymmetry in Ψ can be produced; [Q3] what caused A to be larger in the *Suzaku* observation on average than in that of *NuSTAR*; [Q4] how we can explain the strong EDPV effects in the *NuSTAR* data, and their absence in the *Suzaku* data; [Q5] why the EDPV of the *NuSTAR* data started at $\gtrsim 8$ keV where the SXC still contributes significantly; and [Q6] is the scenario capable of explaining the results from 4U 0142+61 as well. Since the phenomena involved here are all specific to magnetars, we should answer these queries based on astrophysics of strong MFs, with the least amount of ad-hoc ideas that are unrelated to this extreme environment.

5.4.1 Photon splitting process

One promising emission mechanism of the magnetar HXC assumes that gamma-ray photons (including the 511 keV annihilation photons in particular), somehow created near the magnetic poles under the ultra-strong MFs, propagate across the magnetosphere and repeatedly experience, instead of the electron-positron pair creation, a quantum-electro-dynamical process called *photon splitting*; a gamma-ray photon splits into two softer photons, with the aid of the strong MF (*e.g.*, Hu et al. 2019; Enoto et al. 2010b), while conserving the photon energy. The photons thus increase in number but degrade in energy, to form the HXC with very hard spectral slopes. If this process is operating, the emission region will naturally acquire a conical geometry formed by the MFs, although the local directional emissivity would be rather complex, depending on the MF direction and the photon polarization. If the cone is not hollow physically, we may superpose a series of cones with different θ. These affirmatively answer [Q1] at least qualitatively.

5.4.2 Magnetic multipole contributions

The cone would be symmetric around $\hat{x}_3$ if the MF has a pure dipole configuration. However, the MF of a magnetar is usually considered to comprise tilted multipoles (*e.g.*, Thompson et al. 2002; Tiengo et al. 2013; Yao et al. 2018), which are much stronger and no longer symmetric around $\hat{x}_3$. In fact, the characteristic three-peak pulse profiles in Fig. 16e are reminiscent of the 4-peak profile of SGR 1900+14 during its Giant Flare in 1988, which was taken as evidence for a multipolar geometry (Feroci et al. 2002). Then, the local MF intensity B can depend on Ψ. This implies $a > 0$, because the photon-splitting cross section is thought to depend strongly on B and the photon energy E approximately as (Harding & Lai 2008)

$$\sigma_{2\mathrm{p}} \propto E^5 B^6 \ . \tag{21}$$

This will provide a possible answer to [Q2]. Incidentally, based on this dependence, weaker B would lead to a harder HXC slope, because the gamma-ray source photons would then stop splitting at relatively high energies (Enoto et al. 2010b). This mechanism may explain the observed scaling that less active magnetars show harder HXC (§ 3.1).

The intensity and configuration of a magnetar's MF are considered to vary considerably with time, particularly when the activity changes (*e.g.*, Yao et al. 2018). Hence it would be natural to presume that the multipole component of 1E 1547−5408 was stronger during the outburst observation with *Suzaku*. Then, equation (21) predicts that the photon splitting continued to larger distances from the magnetic poles, where the MF opening angle ($\sim \theta$) is larger, and that a was also larger because of the enhanced multipole MFs. This could explain [Q3], *i.e.*, why the modulation amplitude was larger ($A \sim 0.5$ s) in the *Suzaku* data than in the *NuSTAR* data except at $E \sim E_\mathrm{c}$.

5.4.3 Possible proton cyclotron resonance

The most challenging issue is [Q4], namely, how to interpret the EDPV effects which were seen only in the *NuSTAR* data. As suggested by Fig. 5 and Fig. 8, and then confirmed as

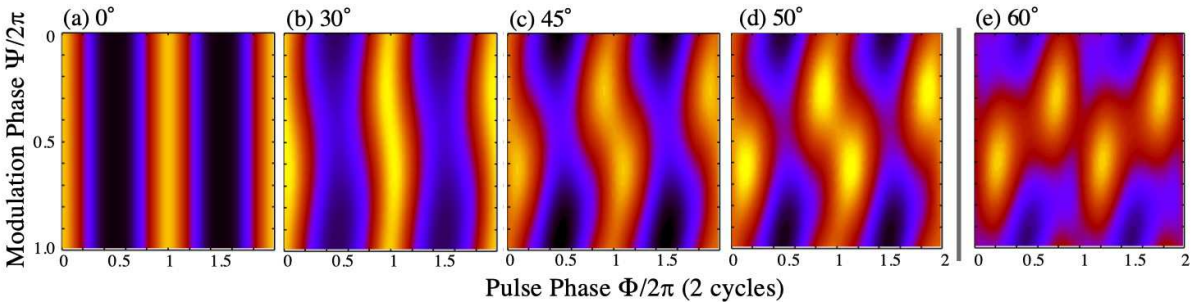

Figure 19. The expected X-ray intensity (corlor), calculated assuming a toy model (see text for details) for several values of θ. The coordinates, $(\Phi/2\pi, \Psi/2\pi)$, are the same as in Fig. 8 and Fig. 12. Panel (e) may be appropriate for the *Suzaku* result in Paper I.

in Fig. 11, $\tilde{A}(E)$ increases sharply at $E_{\rm c} \pm E_{\rm w} = 21.6 \pm 6.9$ keV as if a resonance is operating. As a conceivable resonance phenomenon in magnetars, we speculate that this might be the proton cyclotron resonance in the magnetic poles (Zane et al. 2001), which will take place at an energy of

$$E_{\rm pcr} = 6.3 \times (B/10^{15}{\rm G})(1+z)^{-1} \ \ {\rm keV} \qquad (22)$$

where $z \sim 0.25$ is the gravitational redshift on the NS surface. So far, spectral evidence of the proton cyclotron resonance has been obtained from several magnetars, mostly as (often transient) absorption lines at typical energies of several keV (Rea et al. 2003; Tiengo et al. 2013; Borghese et al. 2015; Chakraborty et al. 2016; Pizzocaro et al. 2019). Then, by setting $E_{\rm pcr} = E_{\rm c}$, we deduce $B = 4.3 \times 10^{15}$ G. Although this is an order of magnitude higher than the nominal dipole MF of 1E 1547−5408, 2.2×10^{14} G (Kuiper et al. 2012), it could be explained by the assumed local multipoles. In fact, it is still an order of magnitude lower than the toroidal field $B_{\rm t} \sim 10^{16}$ G, suggested by the value of ϵ (Paper I).

The resonance width, $E_{\rm w} = 6.9$ keV, may be attributed mostly to the gradients in the MF intensity, because the thermal Doppler broadening must be much smaller, $E_{\rm tD} \sim 0.5$ keV as judging from the SXC temperature (§ 3.1).

Because the Compton cross section is inversely proportional to the scatterer mass, photon scattering by protons is usually negligible compared to that by electrons. However, the electron scattering is completely inhibited in the present case due to the MF (except ordinary-mode photons propagating across the MF lines), whereas the proton scattering must be enhanced resonantly at $E \sim E_{\rm pcr}$, by a factor $(E_{\rm pcr}/E_{\rm tD})^2 \sim 2 \times 10^3$, like in electron-cyclotron resonances (Harding & Daugherty 2008). Therefore, photons with $E \sim E_{\rm pcr}$ would be resonantly scattered by protons with a cross section which is comparable to the Thomson cross section. Since the NS atmosphere is usually considered Thomson thick, a fair fraction of HXC photons with these energies, that are traveling with small angles to the MF lines, would be scattered sideways by protons. This will work as effectively increasing θ, and might explain the energy dependence of $\tilde{A}(E)$, possibly answering the first half of [Q4]. However, admittedly, the explanations of $\tilde{\psi}(E)$ and $S(E)$ are yet to be found. We might need to invoke some exotic physics, because they both *break the basic time-reversal symmetry*, apparently without energy dissipation.

5.4.4 Some thoughts on the SXC vs. HXC relation

In the *NuSTAR* data, the 36 ks pulse-phase modulation was absent at < 8 keV, where the SXC is dominant (Fig. 1). This agrees with the results of Paper I, and those for 4U 0142+61 (Makishima et al. 2014, 2019), indicating that the SXC has a symmetric emission pattern around $\hat{x}_3$. The two spectral components are hence inferred to differ not only in their spectral shapes, but also in their emissivity patterns and production mechanisms. While the HXC possibly results from the photon splitting process, the SXC is likely to be thermal radiation (but modified by the strong MF) from the heated polar regions. Since the two spectral components have comparable luminosities, and there is a hint of variation propagation from the HXC to SXC (§ 3.2), the SXC may be powered via two channels; direct magnetic heating of the polar regions, and heating by the HXC.

With these in mind, let us consider [Q5], for which we can think of at least two possibilities. One is that the hardest end of the SXC also breaks the symmetry around $\hat{x}_3$, and the other is that the phase modulation in the HXC pulses is enhanced at the lowest end of the HXC spectrum. Although the former could work, below we consider the latter scenario. When spin flips of protons in the MF are taken into account, the proton cyclotron resonance would take place not only at $E_{\rm pcr}$, but also generally at (Zane et al. 2001)

$$E_{n,s} = (n + sg/2)E_{\rm pcr} \qquad (23)$$

where n is an integer describing Landau-level separations, $g = 5.586$ is the proton g-factor, and $s = 0$ or ± 1 specifies the spin flips. Equation (22) is the case with $n = 1$ and $s = 0$. Usually, the resonance with $s = 0$ and $n = \pm 1$ has far larger strengths than those with $s = \pm 1$ and $n = 0$, but these conditions might change under the ultra-strong MFs. Then, the observed resonance centre $E_{\rm c}$ could alternatively be identified with $E_{0,1} = 2.79 E_{\rm pcr}$, and if so, the fundamental resonance should occur at $E_{\rm pcr} = 21.6/2.79 = 7.74$ keV, implying $B = 1.5 \times 10^{15}$ G. In this case, $\tilde{A}(E)$ will be enhanced at ~ 7.7 keV, and this effect might partially cancel the decreasing HCX contribution below ~ 12 keV (Fig. 1), making the modulation visible down to ~ 8 keV.

Although the reversal in Ψ is not easily explained, its energy, $E \sim 27$ keV, might fit into the scheme of equation (23). In fact, if assuming $E_{\rm pcr} = 7.74$ keV, we expect $E_{1,1} = 29.4$ keV, which is close to the Ψ-reversal energy, $E_{\rm d}$, considering systematic uncertainties in the model form of $\tilde{\psi}(E)$. The transition with $n = 1$ and $s = \pm 1$ should be forbidden by the

quantum selection rule at least in the 1st order perturbation, but might be allowed in higher orders.

The above interpretation has an obvious caveat; no spectral features (emission, absorption, or break) are seen at any of these characteristic energies. This issue would be our future task, since the proton cyclotron resonance phenomenon under extreme MFs is currently far less understood than the more familiar electron cyclotron resonance in X-ray pulsars (Makishima 2016).

Putting this spectral issue aside, how about these resonances in the *Suzaku* observation, when the pulse-phase modulation amplitude was not apparently energy dependent in $10-40$ keV (Paper I)? It could be that the multipole MF was stronger at that time due to the enhanced activity, so these resonances were at >40 keV where the *Suzaku* HXD data had limited signal-to-noise ratio. An alternative scenario is that the resonances were actually in the 10–40 keV range covered by the HXD, but the effect was not noticeable because θ was already rather large as considered above. These may give an answer to the 2nd half of [Q4].

In a future work, we will return to the *Suzaku* observation, and re-analyse the XIS data in the 5–12 keV range for possible energy dependent pulse-phase behaviour. Also, analyzing the *NuSTAR* data of 1E 1547−5408, acquired in 2019 for a comparable length of time as the present data set, is evidently our another future task.

5.4.5 Comparison with 4U 0142+61

To explain the present *NuSTAR* data of 1E 1547−5408, we have so far developed a scenario which combines such physical ideas as the free precession of a NS that is axially deformed by intense toroidal MFs, the photon splitting process as the HXC emission mechanism, the variable multipole configuration, and the proton cyclotron resonance. Although the scenario is very speculative, the invoked individual ingredients are not extraordinary in view of the basic physics of strong MFs, and of the understanding of magnetars as magnetically-powered NSs. Therefore, the scenario must be able to explain the behaviour of 4U 0142+61 as well.

The $T=55$ ks pulse-phase modulation in 4U 0142+61 has been detected in two out of three observations with *Suzaku*, and one observation with *NuSTAR* (Makishima et al. 2014, 2019). In all the three cases, the effect was observed only in the HXC, and was absent in the SXC, in agreement with the behaviour of 1E 1547−5408. The modulation amplitude of 4U 0142+61 differed considerably from one observation to another; $A/P_0=0.08\pm0.03, 0.14\pm0.05$, and 0.020 ± 0.009 (Table 2 of Makishima et al. (2019)), with $P_0=8.689$ s. These variations in A may be explained by the present scenario as a change of θ, or a, or both.

Since 4U 0142+61 is a much older system, the same mechanism as for [Q2] should explain why 4U 0142+61 showed on average smaller A/P ratios than 1E 1547−5408 in 2009, and than in the present data at $E\sim E_{\rm c}$. Likewise, 4U 0142+61 is thought to have its proton cyclotron resonances much below the HXC energy range. This may explain why none of the three observations of 4U 0142+61 gave evidence of noticeable energy dependence of A. Thus, the scenario is thought to apply to 4U 0142+61 as well [Q6].

Finally, the complex pulse-phase behaviour found in the present data would not be specific to 1E 1547−5408. We expect that similar phenomena will be revealed by detailed hard X-ray timing studies of other magnetars, particularly young and active ones.

6 CONCLUSION

During the *NuSTAR* observation made after 1E 1547−5408 returned in quiescence, the HXC pulses at $P_0=2.08671$ sec were phase-modulated with the same 36 ks period as in the outburst observation with *Suzaku* (Paper I). Because of the presence both in the outburst and quiescence, this 36 ks periodicity can be identified with the slip period, associated with the free precession of the NS that is axially deformed by $\epsilon\sim0.6\times10^{-4}$. The deformation, in turn, is likely due to the internal toroidal MF reaching $\sim10^{16}$ G. The SXC pulses were free from the phase modulation. Therefore, the two spectral components must be distinct in their emissivity patterns, as well as in their spectral shapes.

In the present data, the pulsed fraction was high ($\gtrsim40\%$) below 8 keV, but it decreased to $\lesssim10\%$ in the 10–25 keV interval. This puzzling behaviour was found to stem from strong energy dependences in the HXC pulse properties, partially coupled with the 36 ks phase modulation. Namely, at $E\sim22$ keV, the modulation amplitude exhibited a resonance-like enhancement to $\sim P_0/4$. Over the ~10 to ~27 keV interval, the modulation phase changed by $\sim65^\circ$, followed by a $\sim180^\circ$ jump. Regardless of the 36 ks phase, the overall pulse phase shifted with energy by $\sim8\%$. Corrections of the photon arrival times for these effects have successfully brought the PF to $\gtrsim18\%$ over the entire 8–70 keV range, and rectified the energy-dependent irregular variations in the HXC pulse phase and shape.

Though still tentative and speculative, a possible astrophysical scenario for these unexpected results has been derived. That is, the HXC is produced by the photon-splitting process, and its emissivity is asymmetric around $\hat{x}_3$ due to the presence of tilted strong multipoles. The degree of this asymmetry depends on the energy, possibly due to a proton cyclotron resonance which might be present at ~22 keV or ~7.8 keV, although no spectral features are observed at these energies. In any event, this modeling will provide a useful guideline to future observations (including polarimetry) of this magnetar and similar objects, and to various theoretical studies of physics under extreme MFs.

Our final words should be: "The truth, however strange in itself, is always interesting and beautiful to seekers after it." (quoted and modified from Agatha Christie, *The Murder of Roger Ackroyd*).

ACKNOWLEDGEMENTS

The present work was financially supported by the JSPS grant-in-aid (KAKENHI), number 18K03694.

DATA AVAILABILITY

The data underlying this article are available in the NASA/GSFC HEASARC NuSTAR Data Archive, at https://heasarc.gsfc.nasa.gov/docs/nustar/nustar_archive.html

REFERENCES

Bisnovatyi-Kogan G. S., Moiseenko S. G., Ardelyan N. V., 2018, Phys. Atomic Nuclei, 81, 266
Borghese A., Rea N., Coti Zelati F., Tiengo A., Turolla R., 2015, ApJ, 807, id.L20
Brazier K. T., 1994, MNRAS, 268, 709
Buccheri, R. et al., 1983, A&A, 128, 245
Chakraborty M., Göğüş E., Şaşmaz Mşs S., Kaneko Y., 2016, ApJ, 819, id.153
Coti Zelati F. et al., 2020, A&A, 633, id.A31 (CZ20)
Cowan Glen 1998, Statistical data analysis, Chapter 9, Oxford: Clarendon Press, 1998 Series: Oxford science publications. ISBN: 0198501560
Enoto T. et al., 2010a, PASJ, 62, 475 (Paper I)
Enoto T. et al., 2017, ApJS, 231, id.8
Enoto T., Makishima K., Nakazawa K., Kokubun M., Kawaharada M., Kotoku J., Shibazaki N., 2011, PASJ, 63, 387
Enoto T., Nakazawa K., Makishima K., Rea N., Hurley K., Shibata S., 2010b, ApJ, 722, L162
Feroci M., Hurley K., Duncan R. C., Thompson C., 2001, ApJ, 549, 1021
Halpern J. P., Gotthelf E. V., Reynolds J., Ransom S. M., Camilo, F., 2008, ApJ, 676, 1178
Harding A.K., Daugherty J. K., 1991, ApJ, 374, 687
Harding A.K., Lai D., 2006, Rep. Prog. Phys., 69, 2631
Hu K., Baring M. G., Wadiasingh, Z., Harding, A.K., 2019, MNRAS, 486, 3327
Ioka K., Sasaki M., 2004, ApJ, 600, 296
Iwahashi T. et al., 2013, PASJ, 65, id.52
Kokubun M. et al., 2007, PASJ, 59, S53
Kuiper L., Hermsen W., den Hartog P. R., Collmar W., 2006, ApJ, 645, 556
Kuiper L., Hermsen W., den Hartog P. R., Urama, J. O., 2012, ApJ, 748, id.133
Makishima K., 2016, Proc. Japan Academy, Ser. B, 92, 135
Makishima K., Enoto T., Hiraga J. S., Nakano T., Nakazawa K., Sakurai S., Sasano M., Murakami H., 2014, Phys. Rev. Lett., 112, id.171102
Makishima K., Enoto T., Murakami H., Furuta Y., Nakano T, Sasano M., Nakazawa, K., 2016, PASJ, 68S, id.12 (Paper I)
Makishima K., Muakami H., Enoto T., Nakazawa K., 2019, PASJ, 71, id.15
Mastrano A., Lasky P. D., Melatos A., 2013, MNRAS, 434, 1658
Mereghetti S., 2008, A&ARv, 15, 225
Nakagawa Y. E., Yoshida A., Yamaoka K., Shibazaki, N., 2009, PASJ, 61, 109
Pizzocaro, D. et al., 2019, A&A, 626, id.A39
Rea N., Israel, G. l., Stella, L., Oosterbroek, Y., Mereghetti, S., Angelini, L., Campana, S., Covino, S., 2003, ApJ, 586, L65
Rodriguez Castillo G.A., et al., 2016, MNRAS, 456, 4145
Takahashi T., et al., 2007, PASJ, 59, S35
Tiengo A. et al., 2013, Nature, 500, 312
Thompson C., Lyutikov M., Kulkarni S. R., 2002, ApJ, 574, 332
Thompson C., Duncan R. C., 1995, MNRAS, 275, 255
Yao Guang-Rui, Huang Lei, Yu Cong, Shen Zhi-Qiang, 2018, ApJ, 854, id.10
Yoneda H., 2020, PhD thesis, Department of Physics, The University of Tokyo
Zane S., Turolla R., Stella L., Treves A., 2001, ApJ, 560, 384

APPENDIX A: THE Z^2 STATISTICS

Although the Z^2_m method was originally proposed for unbinned photon-series data (Buccheri et al. 1983; Brazier 1994; Enoto et al. 2011), the algorithm involves photon-by-photon calculations of sinusoidal functions. The Fourier-power scheme of equation (6) provides an equivalent and a faster way, and the results are insensitive to $N_{\rm bin}$ if $N_{\rm bin} \gg m$. In the present analysis, we employ $N_{\rm bin} = 360$.

As m increases and approaches $N_{\rm bin}$, the Z^2_m evaluation becomes equivalent to the chi-square method as predicted by the Parseval's theorem. In this way, the Z^2 technique evaluates the pulse significance using only the lowest several harmonics which usually carry most of the signal power. This makes the Z^2_m method much less subject to the Poisson noise than the chi-square statistics. An additional advantage of the Z^2 technique is that it is essentially free from a natal nuisance in the other method, namely, the choice of $N_{\rm bin}$.

For Poissonian random signals without intrinsic periodicity, the values of Z^2_m obey a chi-square distribution of $2m$ degrees of freedom, and its probability density is given as

$$f(X; 2m) \propto X^{m-1} \exp(-X/2) \tag{24}$$

where Z^2_m is abbreviated as X. The distribution has the mean of $2m$, and the standard deviation of $2\sqrt{m}$ around it. Then,, Z^2_m is expected to increases with m as

$$Z^2_{m+1}(P) \sim Z^2_m(P) + 2\ . \tag{25}$$

When the data contain an intrinsic periodicity at P, its power and the Poissonian contribution approximately add up to make Z^2_m. As a result, the increment $\delta X \equiv X - X_0$ becomes an important measure when conducting the demodulation in § 4. Here, X_0 denotes the value of Z^2_m without demodulation. When using $m = 1$ in particular, equation (25) for the Poissonian contribution becomes an exponential function; so is the upper integral of $f(X; m)$. Therefore, a value of X, which is larger by δX than a fiducial value X_0, has a factor $\exp(-\delta X/2)$ lower chance occurrence probability than X_0. This factor becomes 6.7×10^{-3} if $\delta X = 10$.

APPENDIX B: THE RUNNING AVERAGE

In the present work, pulse profiles and double-folded maps are smoothed with a running average (RA), where we combine three consecutive bins of time series $\{x_n\}$ as $\tilde{x}_n = x_{n-1}/4 + x_n/2 + x_{n+1}/4$, and use $\{\tilde{x}_n\}$ in place of $\{x_n\}$. By suppressing high-frequency noise, the RA reduces the errors associated with each data bin. If $\{x_n\}$ has an average 1-σ error of δx, and if it is independent between the adjacent bins, the 1-σ fluctuation in $\{\tilde{x}_n\}$ becomes $\{(1/4)^2+(1/2)^2+(1/4)^2\}^{1/2}\delta x = \sqrt{3/8}\ \delta x = 0.61\ \delta x$. This estimate holds when $\{x_n\}$ varies mildly with n.

The above form of RA is equivalent to a Fourier filter of $F(k) = \frac{1}{2}\,[1 + \cos(\pi k/k_0)]$, with k the wave number, and $k_0 = N_{\rm bin}/2$ the Nyquist wave number. When this filter is applied to a white-noise signal with the variance $(\delta x)^2$, the output data have a variance as (with $x \equiv k/k_0$)

$$(\delta x)^2 \int_0^{k_0} F(k)^2 dk = \frac{(\delta x)^2}{4} \int_0^1 [1 + \cos(\pi x)]^2\, dx = \frac{3}{8}(\delta x)^2\ ,$$

and a standard deviation by $\sqrt{3/8}\ \delta x = 0.61\ \delta x$.

We confirmed these estimates using an actual X-ray data set, the *Suzaku* XIS data of 4U 0142+61 in 2009 (Makishima et al. 2014). It consists of $N_{\rm bin} = 53,610$ bins of 2-sec counts, with the average of $\langle x_n \rangle = 44.21$ c bin^{-1} and 1-σ scatter of $\delta x = 6.97$ c bin^{-1}. Since $\delta x \approx \sqrt{\langle x_n \rangle} = 6.65$, the data can be regarded as Poisson-dominated, although the source

was pulsing, like in the present data, with a period of 8.69 s. Through the same RA as above, the 1-σ error was reduced to $\delta x = 4.19$ c bin^{-1}, by a factor of $4.19/6.97 = 0.60$ in agreement with the analytic predictions.

APPENDIX C: ERRORS ASSOCIATED WITH THE Z^2 STATISTICS

Consider a data set $\{t_i\}(i = 0, 1, 2, .., N_{\rm tot} - 1)$ comprising $N_{\rm tot}$ photons, where t_i denotes the arrival time of the i-th photon. Let us search the data for a periodicity at a period P, using up to the m-th harmonics of the Fourier power. Using the Fourier coefficients $\{a_k(P), b_k(P)\}(k = 0, 1, .., m)$ in equation (5) which can be computed by a Fourier transform of $\{t_i\}$, we can construct a scalar quantity, called likelihood function and denoted as $L[t_i; \{a_k(P), b_k(P)\}; P]$, which expresses the probability for the data to have a periodicity at P. The best-estimated period is obtained as a value of P that maximizes this likelihood. In a more complex analysis (*e.g.*, the demodulation analysis), L may depend not only on P, but also on some other parameters. In this case, L must be maximized with respect to all these parameters.

When the time series is dominated by the Poisson noise, there holds a relation as (Yoneda 2020)

$$\ln L[t_i; \{a_k(P), b_k(P)\}; P] \approx \frac{1}{2} Z^2_m \ . \tag{26}$$

Therefore, the demodulation analysis, where we search for the maximum Z^2_m, is equivalently to maximizing the log likelihood with respect to the four parameters, P, A, T, and ψ.

In the period search using the chi-square method, the errors associated with the best-estimated P (and other parameters) are generally difficult to estimate, because this is suited to a *minimisation* process, and a large value of chi-square is useful only in rejecting a null hypothesis that the signal does not have a significant periodicity at P. In contrast, the Z^2_m evaluation, being a maximizing process, allows the parameter errors to be more easily formulated.

Suppose that a solution (P, T, A, ψ) gives the maximum likelihood, L^*. The true parameters may be slightly different, and so is the associated L_0. Again assuming the noise dominance, the difference $2(\ln L^* - \ln L_0)$ is known to obey a chi-square distribution with ν d.o.f. (Cowan 1998). Here, ν is the number of parameters involved in L. Combining this with equation (26), we find that the values of Z^2_m around its maximum should obey, in the present case, a chi-square distribution with $\nu = 4$. (This 4 represents the parameter number, but not our choice of $m = 4$.) Since its upper 68% probability point is 4.72, we define the 68% error range of each parameter (with the other 3 parameters re-adjusted) as the point where Z^2_4 decreases by 4.72 from the maximum.

APPENDIX D: STATISTICAL SIGNIFICANCE OF THE PULSE-PHASE MODULATION

Following Paper I and Makishima et al. (2019), we evaluated the statistical probability $\mathcal{P}$ with which the 36 ks peak in the 8–25 keV DeMD (Fig. 7) appears due to chance fluctuations. For this purpose, we performed the $m = 4$ demodulation analysis using the same 8–25 keV data, but over a range of $T = 0.25 - 4.0$ ks, where the pulse-phase fluctuation would not have any enhanced periodicity, because the range is much longer than P_0 but shorter than the orbital period of *NuSTAR*, 5.8 ks. We utilised the same scan ranges and steps in P, A, and ψ, as in Fig. 7. To make the adjacent sampling points in T mutually independent in terms of Fourier wave numbers, the scan step in T was varied so as to satisfy $\Delta T \sim T^2/T_{\rm tot}$ where $T_{\rm tot} = 151$ ks is the total observation span. This has yielded 476 steps in T, and in two cases among them, Z^2_4 exceeded the target value of $Z^2_4 = 72.95$ (Table 1). Therefore, the probability of finding Z_4 values larger than was observed, *at a single value of* T, is estimated as $2/476 = 4.2 \times 10^{-3}$.

To obtain $\mathcal{P}$, we must multiply with the effective number of trials $N_{\rm tr}$ in T that was involved in analyzing the actual data. We may set as $N_{\rm tr} = 1$, because our purpose is to reconfirm the *Suzaku* discovery rather than finding a new modulation period, and the error range of equation (4), 7.0 ks, is covered by a single Fourier wave number which haa $\Delta T = 8.5$ ks for $T = 36$ ks. We then obtain $\mathcal{P} \sim 4.2 \times 10^{-3}$. However, this could be an underestimation, because we may have to select $\Delta T \sim 2.1$ ks considering the use of $m = 4$.

To avoid the above ambiguity in $N_{\rm tr}$ that arises via the use of $m > 1$, we repeated the same calculation using $m = 1$ this time. Out of the 476 trials, we again found two cases (but at different values of T from those found with $m = 4$) wherein Z^2_1 exceeded the target value of $Z^2_1 = 60.88$ (Fig. 7). We hence reconfirm $\mathcal{P} \sim 4.2 \times 10^{-3}$. Furthermore, a sort of Monte-Carlo simulation using the actual data instead of fake data, described in Paper I and Makishima et al. (2019), yielded 11 cases, out of 2000, wth Z^2_1 higher than 60.88. This gives $\mathcal{P} \sim 5.5 \times 10^{-3}$. From these evaluations, we quote, as a round number, $\mathcal{P} = 0.5\%$.